Determination of depositional environment and luminescence dating of Pleistocene deposits in the Biely Váh valley, southern foothills of the Tatra Mountains, Slovakia

Ingrid Bejarano

Dissertations in Geology at Lund University,
Master's thesis, no 588
(45 hp/ECTS credits)

Department of Geology
Lund University
2020

Determination of depositional environment and luminescence dating of Pleistocene deposits in the Biely Váh valley, southern foothills of the Tatra Mountains, Slovakia

Master's thesis
Ingrid Bejarano

Department of Geology
Lund University
2020

Table of contents

1 Introduction **9**
2 Geological Setting **9**
3 Theoretical Background **11**
3.1 Luminescence Dating 11
3.1.1 Equivalent Dose and Dose Rate 11
3.1.2 Optically Stimulated and Infrared Stimulated Luminescence 11
3.1.3 Single Aliquot Regenerative-Dose (SAR) Protocol 12
3.1.4 Quality Tests 12
3.2 Luminescence Dating on Quartz 13
3.3 Luminescence Dating on Feldspar 13
3.3.1 Anomalous Fading 13
4 Methods **13**
4.1 Fieldwork 13
4.2 Sedimentology 14
4.2.1 Logging 14
4.2.2 Sampling for clast shape and Maximum particle size 15
4.3 Luminescence dating 15
4.3.1 Sampling 15
4.3.2 Preparation of the Samples 15
4.3.3 Measurements and Data Analysis 16
4.3.4 Age estimation 19
5 Results **20**
5.1 Sedimentology 20
5.1.1 Bee Pit Lower Section 20
5.1.2 Bee Pit Upper Section 21
5.1.3 Clast Shape and Maximum Particle Size 24
5.2 Luminescence dating 25
5.2.1 Measurements on Quartz 25
5.2.2 Measurements in Feldspar 26
5.2.3 Dose Rate and Age Calculation 27
6 Discussion **29**
6.1 Sedimentology and Depositional Processes 29
6.2 Luminescence dating with OSL and IRSL 31
6.2.1 OSL dating issues 31
6.2.2 Water content 31
6.2.3 Anomalous fading 32

6.2.4 Determination of the ages 33
6.3 Depositional History 33
7 Conclusions 34
8 Acknowledgments 35
References 36
Appendixes 40

Cover Picture: Panoramic view of the lower section of the gravel pit, where the study was done.

Determination of depositional environment and luminescence dating of Pleistocene deposits in the Biely Váh valley, southern foothills of the Tatra Mountains, Slovakia

INGRID BEJARANO

Bejarano, I., 2020: Determination of depositional environment and luminescence dating of Pleistocene deposits in the Biely Váh valley, southern foothills of the Tatra Mountains, Slovakia.
Dissertations in Geology at Lund University, No. 588, 41 pp. 45 hp (45 ECTS credits).

Abstract: The Tatra mountains have had several glaciations during the Quaternary. The deposits located in the southern foothills were classified as glaciofluvial, based on geomorphology, but its sediments have not been studied in detail. Therefore, this project focused on establishing the depositional history, processes and age of the deposits in a gravel pit, located in the Biely Váh valley in these foothills. The combination of luminescence dating with sedimentological analysis, including clast shape and maximum particle size, were the methods of choice. For the luminescence dating eleven samples were collected from the units composed mainly of sand.

Initially optically stimulated luminescence (OSL) dating was used, but after applying the standard Single Aliquot Regeneration (SAR) protocol quality tests, it was evident the quartz was poorly behaved with low signal intensity. The dose estimation gave bad results, even after attempting pulsed OSL and differential OSL. Therefore, it was decided to move on to feldspar grains. Given that there is a risk of fading and the fact that feldspar grains take longer to bleach, the corrective measurements were done by calculating the g-value and use of IR_{50} and $pIRIR_{225}$ signals for the bleaching.

The sedimentological description yielded 13 units from the lower and upper outcrop in the study area. The results of sedimentological analysis indicated that the process of deposition had a high energy component, representative of subaerial sediment-water flows. Given the features of the sediments it was identified as a hyperconcentrated flow. Moreover, for the age determination the most likely water content of the sediments was chosen, the g-values and the equivalent dose were determined, using both IR_{50} and $pIRIR_{225}$ signals. Subsequently, four ages were obtained per sample, one for each signal, and with and without correction for fading. From these, the uncorrected $pIRIR_{225}$ ages were selected, since this signal has a lower fading rate which is supported by the obtained g-values, which were smaller than 1-1.5%.

The results were compared to the known glacial history of the Tatra mountains. The obtained luminescence ages, which range from ca 200 to 260 ka, would correspond to the Riss glaciation. Both ages and sediment characteristics match those of the other deposits from the northern and southern Tatra foothills that also have been correlated to the Riss glaciation. Taken together, these results suggest a glacial advance to the present-day foothills of the High Tatras during the Riss glaciation and extensive deposition of glacifluvial sediments outside the ice margin.

Keywords: Luminescence dating, glacifluvial deposits, sedimentological analysis, High Tatra Mountains, IRSL dating.
Supervisor: Helena Alexanderson.
Co-supervisors: Isa Doverbratt and Juraj Janočko

Subject: Quaternary Geology

Ingrid Bejarano, Department of Geology, Lund University, Sölvegatan 12, SE-223 62 Lund, Sweden.
E-mail: ingridbejarano.geo@gmail.com

Bestämning av avsättningsmiljö och luminiscensdatering av Pleistocena sediment i Biely Váh-älvens dalgång, Tatrabergens sydsluttning, Slovakien

INGRID BEJARANO

Bejarano, I., 2020: Bestämning av avsättningsmiljö och luminiscensdatering av Pleistocena sediment i Biely Váh-älvens dalgång, Tatrabergens sydsluttning, Slovakien
Examensarbeten i geologi vid Lunds universitet, Nr. 588, 41 sidor. 45 hp (45 ECTS).

Sammanfattning: Tatrabergen, som ligger i västra delen av Karpaterna, har upplevt flera nedisningar under kvartärtiden. Avsättningarna i sluttningarna längs bergens södra sida har klassificerats som glacifluviala, baserat på geomorfologi, men har inte undersökts i detalj tidigare. Det här projektet fokuserar därför på att etablera avsättningshistoria och -processer samt avlagringarnas ålder i ett grustag i Biely Váh-dalen som skär genom dessa sluttningar. En kombination av luminiscensdatering och sedimentologisk analys, inklusive partikelform och maxpartikelstorlek (MPS), har använts. Elva prover från sandiga enheter samlades in för luminiscensdatering. Partikelanalys genomfördes i de grövre enheterna som innehöll sten och block.

Till en början användes optiskt stimulerad luminiscensdatering (OSL), men efter att ha tillämpat de kvalitetstester som ingår i ett standard *Single Aliquot Regeneration* (SAR) protokoll stod det klart att kvartsen hade dåliga luminiscensegenskaper med låg signalintensitet. Dosmätningarna gav dåliga resultat, även med pulserad OSL och differentiell OSL. Det blev därför bestämt att fortsätta mätningarna på fältspat istället. Eftersom det finns risk för s.k. *fading* och eftersom fältspatkorn tar längre tid på sig att nollställas, korrigerades resultaten med hjälp av uppmätta g-värden och nollställningen utvärderades genom att se på signalerna från både IR_{50} and $pIRIR_{225}$.

Genom den sedimentologiska beskrivningen identifierades tretton enheter från den nedre och övre skärningen i undersökningsområdet. Resultaten av de sedimentologiska analyserna visade att avsättningen skedde i en miljö med hög energi genom subaerila sediment-vattenströmmar, utifrån sedimentegenskaperna klassificerade som hyperkoncentrerade strömmar. För åldersberäkningen bestämdes den sannolika vattenkvoten hos sedimenten, och g -värden och ekvivalent dos bestämdes för både IR50 and pIRIR225 signalerna. Därefter beräknades fyra åldrar per prov, en för varje signal och med respektive utan korrektion för fading. Från dessa valdes de okorrigerade pIRIR225 åldrarna, eftersom denna signal nollställs snabbare än andra pIRIR-signaler och har en lägre fading rate än IR50. Flera av proverna hade doser som var nära mättnad eller var mättade.

Resultaten jämfördes med den tidigare beskrivna glaciationshistorien för Tatrabergen. Luminiscensåldrarna, som spänner från ca 200 till 260 ka, skulle motsvara Riss-glaciationen. Både åldrar och sedimentegenskaper motsvarar de hos andra avsättningar från norra och södra sidan av Tatrabergen och som också har korrelerats med Rissglaciationen. Tillsammans visar dessa resultat på en isframstöt till de nuvarande sluttningarna av Höga Tatra under Riss-glaciationen och att stora volymer glacifluviala sediment avsattes utanför iskanten.

Nyckelord: Luminiscensdatering, glacifluviala sediment, sedimentologisk analys, Tatrabergen, IRSL-datering.
Handledare: Helena Alexanderson.
Biträdande handledare: Isa Doverbratt och Juraj Janočko

Ämnesinriktning: Berggrundsgeologi

Ingrid Bejarano, Geologiska institutionen, Lunds universitet, Sölvegatan 12, SE-223 62 Lund, Sverige.
E-mail: ingridbejarano.geo@gmail.com

1 Introduction

The Tatra Mountains are located in central Europe, in the northernmost part of the Western Carpathians (Figure 1), which are divided into three principal zones – the External Western Carpathians (EWC), the Central Western Carpathians (CWC), and the Internal Western Carpathians (IWC) (Králiková et al. 2014). Likewise, they are the highest massif in the Carpathian mountain arc (2655 m) and represent a typical alpine landscape that has developed in the course of Pleistocene glaciations, but is not glaciated today (Kłapyta et al. 2016). Hence, there have been many studies in the last decades in the Tatra Mountains, focusing on trying to unravel its glacial history, given the fact that there is still lots to be understood (e.g. Lindner et al. 2003; Makos et al. 2013; Králiková et al. 2014; Kłapyta et al. 2016).

The study area is set in the southern foothills of the Tatra Mountains, on the Slovakian side which has not been studied extensively. Landforms in the area are classified as glacifluvial terraces based only on the previously done mapping (Lindner et al. 2003; Zasadni & Kłapyta 2014; Zasadni et al. 2020). These deposits have few analyses to verify this classification, like dating or sedimentological studies (Zasadni & Kłapyta 2014; Makos 2015). Likewise, the chronology of the four identified stadials of the last glaciation and the age of the till cover were proposed only based on morphostratigraphy but no numerical dating analyses were performed (Zasadni & Kłapyta 2014). The gaps in the information leave important questions to be answered and make them the aim of this thesis project. What is the depositional history of the area of study? Specifically, how were these deposits formed? Which were the processes that shaped the foothills? As well as determining the age of these deposits and their stratigraphy. Consequently, the glacifluvial deposits located in the southern foothills of the Tatra Mountains, on the Slovakian side, are the focus of this study. More specifically, in a gravel pit located at the Biely Váh river, referred to as the Bee Pit (Figure 1).

The methods that have been used to achieve this project's objectives are luminescence dating and sedimentological analysis. Luminescence dating offers a method to date sediments that were exposed to daylight, indicating when the grains were last exposed (Duller 2008). This is done based on the radioactivity, from naturally occurring isotopic elements such as Uranium and Thorium, received by quartz and/or feldspar grains within the samples. This method is well suited to date the glacifluvial deposits found in the study area, which are composed mainly of sand. Thus, for the luminescence dating eleven samples were collected from a gravel pit, located in the southern foothills of the Tatra Mountains, in the Biely Váh valley. The sedimentological analysis comprises the structure and texture of the sediments, along with clast shape analysis and maximum particle size. These datasets provide information about transport paths and depositional processes that the sediments had concerning the shape of the clasts. Therefore, the sedimentological analysis complements the dating method to find evidence that would determine the depositional environment of these sediments.

2 Geological Setting

The Tatra Mountains cover an area of 785 km^2 and share the border between Slovakia to the south and Poland to the north (Králiková et al. 2014). They are divided into three areas according to their geological structure and relief, the Western Tatras, the High Tatras (southeast), and the Belianske (northeast). The Western Tatras are composed of metamorphic, crystalline and sedimentary rocks, which are characterised by a glacial relief that is confined predominantly to the metamorphic and crystalline part, making the highest area in the south. The High Tatras comprise granites with a typical alpine-type glacial relief and the Belianske Tatry is constituted by sedimentary rocks with small cirques, which slightly modify the landscape (Figure 2). The uplift that occurred during the Neogene along the Sub-Tatra fault tilted the massif towards the north, creating a distinct asymmetric slope resulting in steeper profiles of the southern valleys, and the base of the valley-head cirque basins being

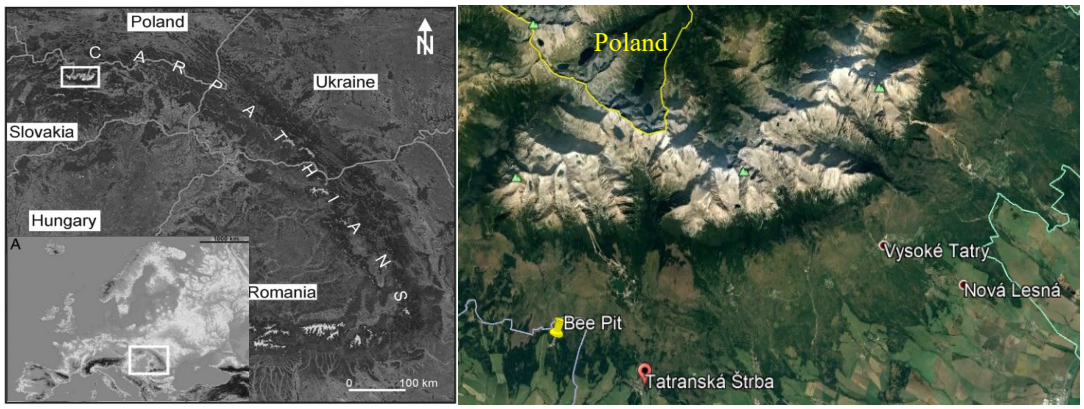

Figure 1. Localisation map of the Tatra Mountains in Europe, Slovakia and the study area, Bee Pit. Modified from Makos et al. (2014), Makos et al. (2013) and google maps.

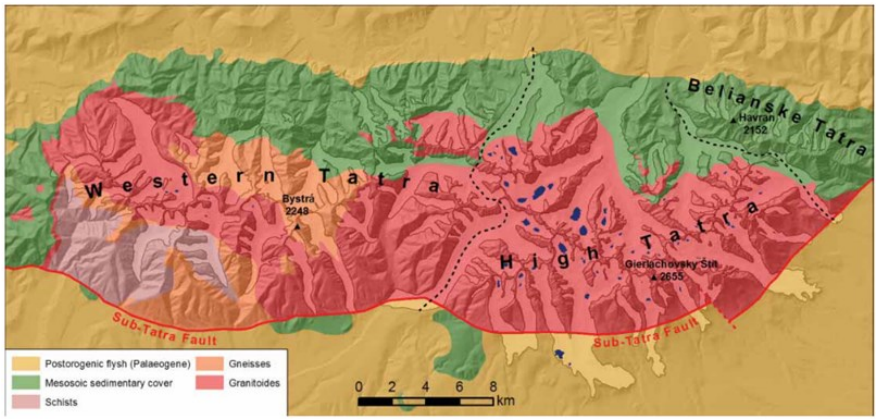

Figure 2. Geological map with the geographic subdivision of the Tatra Mountains. The dashed lines illustrate the division of the Tatras into three geographic regions, taken from Zasadni & Kłapyta (2014).

more elevated than in the north (Zasadni & Kłapyta 2014).

The regional geology of the Tatra Mountains has been described by Králiková et al. (2014). They state that the core is formed by the Tatric crystalline basement, composed of two thick-skinned Variscan tectonic units: the Jalovenic being the lower one, and the Baranec Unit being the upper one. The Jalovenic is described as a complex unit of schists and gneisses with intercalations of quartzite. The Baranec unit is constituted of metamorphic rocks such as migmatite, orthogneiss, paragneiss among others, and the main mass comprises different types of Variscan granites. During the Late Permian to Cretaceous the Tatric sedimentary cover was formed. It displays a monoclinal structure and presents a northward inclination with a thickness that ranges from several hundred meters to a maximum of ~2000 m. Overriding the Tatric unit are Mezosoic nappes from the Veporic unit which are composed of carbonate rock and these nappes are divided into the Fatric nappes (lower) and Hronic nappes (upper). The Fatric unit's age ranges from Early Triassic to Early Cretaceous and the Hronic unit is Middle Triassic to Early Jurassic. The nappes are the substratum of the Central Carpatic Paleogene Basin (CCPB), a sedimentary succession of Eocene to earliest Miocene in age. Also known as the Podtatranská skupina Group, it is composed of deep-marine siliciclastic material with up to 4 km in thickness. It is divided into four formations Borové, Huty, Zuberec, Chocholów, and Biely potok (Appendix A). Lastly, Quaternary sediments and landforms can be found in significant amounts in the southern foothills of the High Tatra Mountains, with Pleistocene moraines and glacifluvial sediments with more than 400 m in thickness. These sediments were deposited in a graben which was related to the normal fault occurring along the Ružbachy and sub-Tatra faults.

The collection of geomorphological and geological data suggests that there were eight glaciations in the Tatra Mountains throughout the Quaternary. During the last glacial maximum, the Tatras were located between the Scandinavian Ice Sheet´s southern border and the eastern part of the Alpine ice cover (Figure 3) (Zasadni & Kłapyta 2014). As stated by Lindner et al. (2003), the evidence of glaciations was found from the presence of glacifluvial deposits at different altitudes with varying ages, and in some cases also in the form of terminal and lateral moraines. Likewise, they mention that throughout the Würm glaciation a remarkably extensive glaciation took place in the Tatra Mountains, compared to previous ones which were limited. This big development of glaciers seems to reflect the long-term western and north-western atmospheric circulation, which conveyed an increase in precipitation favouring the growth of the ice. Also, it is mentioned that leftover dead-ice blocks remained in the higher cirques of the

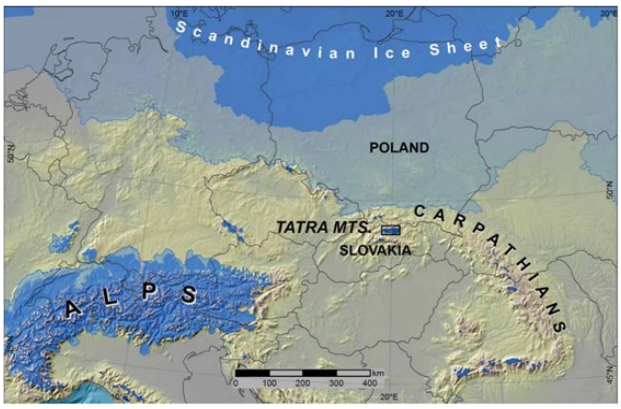

Figure 2. Geological map with the geographic subdivision of the Tatra Mountains. The dashed lines illustrate the division of the Tatras into three geographic regions, taken from

Tatra Mountains during the Late Glacial up until the pre-optimal part of the Holocene.

Moreover, a stratigraphic sequence for the High Tatras was constructed based on morphostratigraphic principles, Schmidt Hammer tests and glacier equilibrium line altitude (ELA) estimation, with three main glacial advances Popradské pleso (Pp) being the oldest, followed by Suchá važecká I (Sv I) and Suchá važecká II (Sv II).

The data collected by Zasadni et al. (2020) shows that the oldest and middle advances (Pp and Sv I) occurred during the Oldest Dryas. The Sv I occurred before the Bølling-Allerød (B/A) warming at 14.9 ± 0.4 ka, when the lower glacial cirques located in the SW part of the High Tatras were occupied by glaciers. The evidence for the Sv II advance shows that the youngest moraines and relict rock glaciers in the Tatra Mountains were formed during the Younger Dryas.

Additionally, Hanzel et al. (1984) described that the Quaternary sediments located in the southern part of the Tatra Mountains, are part of several genetic types classified as polygenic accumulations, fluvial, glaciofluvial and glaciogenic, from the Würm, Riss, and Mindel glaciations. These sediments are characterised by having extremely variable grain sizes and their age span is from the Pleistocene to the Holocene. Furthermore, the thickness of the Quaternary sediments is controlled by the topography of the pre-Quaternary basement and with the analysis of hydrogeological boreholes it was identified that the thickest sediments range from 1.5 to 4 km. Towards the SE of the foothills the thickness of the sediments decreases in the Biely Váh valley where the bedrock of Mesozoic and Paleogene age crops out.

3 Theoretical Background

3.1 Luminescence Dating

Radioactivity occurs naturally in the environment and luminescence dating uses the occurrence of this in the radioactive isotopes of elements like uranium, thorium, and potassium. Subsequently, minerals like quartz and feldspar naturally serve as dosimeters of the amount of radiation to which they have been exposed to. When these minerals have been exposed to the emission of radioactive decay, they have the property of storing a small portion of the energy in their crystal structure. This energy accumulates as exposure to radioactive decay continues over time and later in time this energy may be liberated as light, which is called luminescence (Figure 4). The useful thing about this phenomenon is that it can be reset to zero by two procedures: by heating above 300°C and by the exposure of the minerals to daylight. This occurs naturally for sediments through erosion, transport and deposition (Duller 2008). This event of releasing the previously stored energy is what is measured with luminescence and translated into age by calculating the equivalent dose and dividing it by the dose rate.

3.1.1 Equivalent Dose and Dose Rate

The equivalent dose (D_e) corresponds to the amount of radiation the sample was exposed to during the burial time and it is given in Gray (Gy), which is the unit for absorbed radiation (Duller 2008). Additionally, the D_e is determined by recording the sample's emitted luminescence intensity versus the increasing dose given in the laboratory with ionising radiation from a calibrated

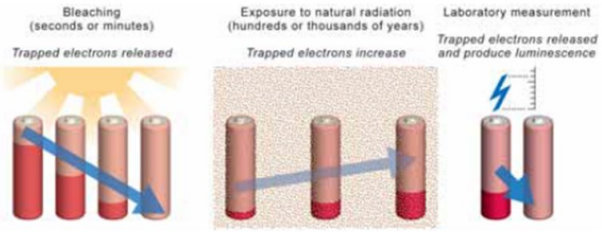

Figure 4. Analogy with a rechargeable battery to show luminescence dating. A) The grains get bleached when exposed to daylight or to heat the electrons are released. B) For a long *period of time, the new exposure recharges the mineral grains and C) in the laboratory the grains are stimulated and their energy is released in form of light. Modified from Duller (2008).*

Beta source ($^{90}Sr/^{90}Y$) (Bateman 2019). The term equivalent dose refers to the fact that laboratory radiation used to construct the dose response of a sample is done only with beta particles, whereas in nature the absorbed radiation comes from both alpha and beta particles, along with gamma and cosmic rays (Huntley 2001).

The dose rate (D_r) consists of the amount of radiation that the sample collects from the surrounding sediments per year. It is calculated from the radioactivity of the elements that occur naturally in the environment subsurface, like U, Th and K. Some of the components that need to be quantified are the radiation emitted by the naturally occurring radioactive nuclides and the water content which absorbs part of the emitted energy to the sample. The D_r of a sample can be calculated if the nuclide concentration of the surrounding sediments is known and the most common method to do so is to count the number and type of particles emitted when they are placed on a detector of known values (Bateman 2019). Each emitting nuclide has a characteristic gamma ray energy and this is used in gamma spectrometers, which count the number of gamma rays in defined energy intervals. Then, these counts are compared with reference materials of well-known nuclides concentrations, allowing to determine the nuclide concentrations of the unknown sample (Knoll 1979). Taking the D_e and D_r into account, the age corresponds to the duration of time that the sample has been receiving the energy. The corresponding formula is given in Gy for the equivalent dose and Gy/ka for the dose rate as follows.

$$Age = \frac{Equivalent\ Dose\ (Gy)}{Dose\ Rate\ (\frac{Gy}{ka})}$$

3.1.2 Optically Stimulated and Infrared Stimulated Luminescence

The luminescence stimulation given to the sample depends on the mineral that is going to be studied and the age range of the sample. The term "OSL dating" was established in 1985 and has been used broadly since on any other luminescence technique apart from thermoluminescence (TL), but it can be limited to the use of

stimulation from blue and green visible light. On the other hand, stimulating with photons in the infrared range leads to the emission of infrared-stimulated luminescence (IRSL) (Aitken 1998).

The most commonly used minerals for luminescence dating are quartz and feldspar, which are naturally exposed to different dose rates and hence record different doses. Therefore, for accurate dosimetry their signals must be separated (Ankjærgaard et al. 2010). The blue light emitting diodes (LEDs) are used to stimulate quartz and infrared light emissions are used to stimulate feldspar. The OSL technique allows to detect at shorter wavelengths than the ones used for stimulation, so quartz is detected with ultraviolet wavelength and feldspar with blue wavelengths (Bateman 2019).

3.1.3 Single Aliquot Regenerative-Dose (SAR) Protocol

As OSL became more popular, there was a need to develop a method to simplify the technique of measuring the D_e where all the measurements could be done with single aliquots. The aliquots are made with stainless steel discs containing a few tens to hundreds of grains of a sample that are attached to the discs with silicone oil (Buylaert et al. 2009).

The single aliquot regenerative-dose (SAR) protocol was developed for OSL by Murray & Wintle (2000). This protocol consists of measuring the natural signal of the grains followed by several repeated cycles that measure the irradiation with increasing doses to create a regenerative dose reply in the aliquots. Before each repeated cycle is made the sample is preheated to empty the thermally unstable traps, which are recharged when the sample is irradiated in the laboratory, and not affecting the thermally stable traps. The SAR protocol controls the OSL response of the samples to a small radiation dose which is given at the end of the regenerative cycles (Table 1). Also, it includes a series of tests that are applied to the samples to check their suitability for the procedure (Murray & Wintle 2000; Murray & Wintle 2003). Since 2000, it has become the method of choice for the measurement of D_e and proven to give accurate results when it is applied correctly (Duller 2008).

Table 1. The sequence illustrates a generalized single-aliquot regeneration (SAR) protocol as proposed by Murray & Wintle (2000).

Step	Treatment[a]	Observed[d]
1	Give dose, D_i	–
2	Preheat[b] (160–300°C for 10 s)	–
3	Stimulate[c] for 100 s at 125°C	L_i
4	Give test dose, D_t	–
5	Heat[b] to 160°C	–
6	Stimulate for 100 s at 125°C	T_i
7	Return to 1	–

3.1.4 Quality Tests

Pre Heat Plateau Test (PHP) - This test determines the appropriate pre-heat temperatures to avoid the measurement of thermally unstable traps (Murray & Wintle 2000). The PHP is done with several aliquots for each one of the different pre-heat temperatures to calculate the average dose. A plateau is identified where the measured dose looks constant, irrespective of temperature (Figure 5A).

Dose Recovery Test- For this test the aliquots are bleached beforehand, which removes all the trapped electrons from the sample, followed by giving them a known dose in the laboratory (Duller 2008). Then, the dose is measured using different preheat temperatures and treated as unknown. The aim is to measure if the known laboratory dose that was given can be determined accurately, and the ratio of measured to given dose should be close to 1 (Figure 5B) (Wintle & Murray 2006).

According to Duller (2003), further tests are applied to all the aliquots to estimate if they are reliable for the age calculation or not, and these are the Recuperation, Recycling and IR depletion.

Recuperation Test- The luminescence signal is measured without prior irradiation and if a signal is observed, it is an unwanted result of the heating steps in the measurement procedure. The recuperated signal should be less than 5% of the natural signal.

Recycling test- It is a test of the sensitivity correction where the sample is given a regenerative dose and then measured. The ratio from the first and the repeated

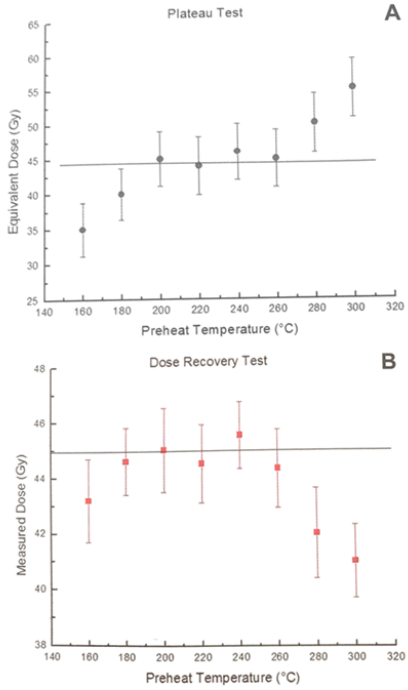

Figure 5. Example of a pre-heat plateau and dose recovery tests. A) The PHP is observed from 200°C to 260°C, for 45 Gy. B) For the temperatures from 180°C to 260°C the dose of 45 Gy is within the bars of error limits; modified from Bateman (2019).

measurement should not deviate more than 10% from each other, between 0.9 and 1.1 is acceptable (Rhodes 2011).

3.2 Luminescence Dating on Quartz

Recently, OSL has experienced a rapid expansion in use for dating quartz sand, especially on younger sediments. It can be used in many areas of the world and environmental sciences (Rhodes 2011). OSL dating is preferably done with quartz due to its high resistivity to weathering, the luminescence signal is reset more quickly in daylight than feldspar and it is not affected by anomalous fading. Nevertheless, quartz has some disadvantages like relatively low luminescence intensity, the luminescence saturates at lower radiation doses and the thermal transfer may be high (Lian 2007). The low saturation dose of the OSL in quartz, about 150 Gy, sets a boundary in the dating age range to < 150,000 years (Bateman 2019).

3.3 Luminescence Dating on Feldspar

Even though the luminescence dating is done preferably with quartz, there are some advantages to do it with feldspar instead. Feldspar saturates at higher radiation doses; the luminescence intensity may be higher and the IRSL stimulation can be done especially in samples with a mix of quartz and feldspar. Feldspar can go further back in time than quartz, up to 200,000 to 300,000 years. The disadvantages are that the weathering of the grains occurs faster, the bleaching is slower and it has the anomalous fading which must be corrected (Lian 2007).

Among the measurements that are done on feldspar grains are the previously mentioned quality tests and the equivalent dose. In order to measure the equivalent dose in the feldspar, the test doses are carried out the same way as for quartz grains. In the test dose however, their IRSL signal is measured instead of the OSL signal. This is all done in the series of measurements that compose the SAR protocol (Duller 2008), including the residual dose measurement which is related to the residual population of trapped electrons. This may remain in the grains even after it has been bleached for a long time (Rhodes 2011). These residual doses could be caused partly by thermal transfer and it is measured by exposing the samples to daylight and then measure to check if there is still some luminescence signal left.

3.3.1 Anomalous Fading

The fading is the loss of signal that occurs over time which cannot be explained as a result of thermal influence. The correction method as proposed by Huntley & Lamothe (2001) quantifies this by the g-value. It measures the percentage of the loss of IRSL signal after the samples had been stored at room temperature, during different periods and receiving a laboratory dose. By doing so, the age underestimation produced by the IRSL fading can be corrected (Aitken 1998). In addition to this, the use of post IR-IRSL (pIRIR) signal, was found to help reduce the fading considerably, permitting the estimation of a reasonable age (Thomsen et al. 2008). The pIRIR consists of an extension to the IRSL stimulation, done above room temperature (50°C-60°C) providing thermal stability, by repeating it with higher temperatures such as 225°C (Buylaert et al. 2009).

4 Methods

4.1 Fieldwork

The fieldwork was carried out for two weeks in August 2019 in the southern foothills of the High Tatra Mountains, near Tatranská Štrba, Slovakia. On the first day of work, the area of study was chosen among two gravel pits that were available and was named the Bee Pit (Figure 6), since there was an apiculture place next to it. The study area is divided into two sections (upper and lower) because the gravel pit was excavated on different levels and the chosen sections have around 20 m difference in between them. The main section is located in the lower pit, it was studied with more detail than the upper one since it was more accessible from the ground level. Consequently, the layers were easier to clean than on the other sections, exposing the different beds more clearly. The following days were invested in the general characterisation and description of the identified units, starting in the lower pit and then in the upper section, which had access through a road that was cleared out when the gravel pit was active (Figure 7).

Subsequently, a general sketch and a sedimentary log were drawn from the cleaned areas in the outcrop, identifying units where the OSL samples would be taken, specifically from the units composed of sand. Likewise, samples were taken for sedimentological analysis for clast shape and maximum particle size, from the units that encompass coarser grains sizes such as pebbles, cobbles and boulders. Once the sand units were identified, the objective was to sample all of them, with at least one sample per unit or more if possible. It was feasible to sample all the sand units with extra samples for two units, one from the upper and another from the lower section, with a total of eleven OSL samples (see Appendix B). The water content samples were taken from the same unit and as close as possible to the OSL tube, for all samples as well. Coordinates were taken to know the location of the Bee Pit and for each sample, with a handheld GPS (Garmin etrex 30).

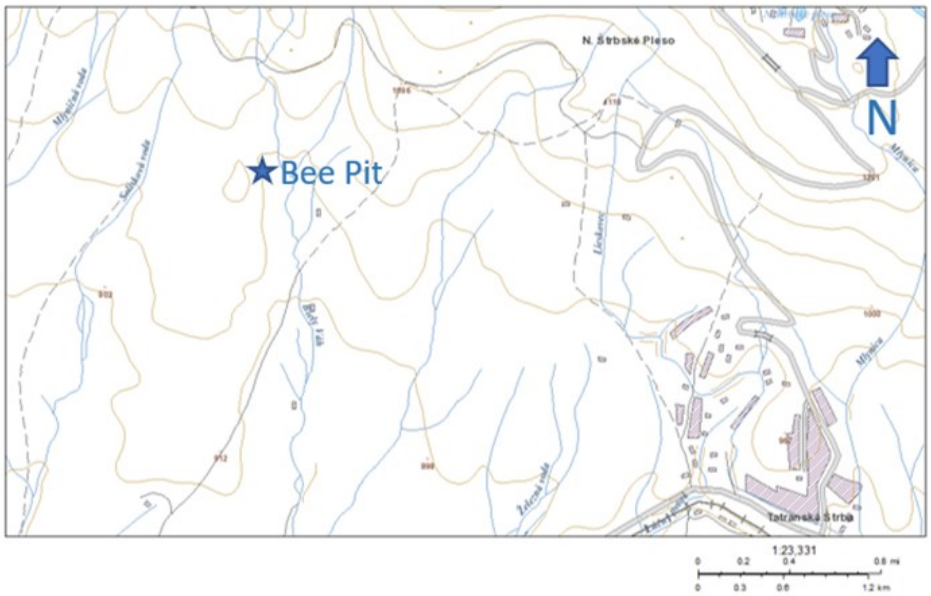

Figure 6. Location of the area of study, Bee Pit located in the blue star, situated in the southern foothills of the Tatra Mountains and near the Biely Váh river valley.

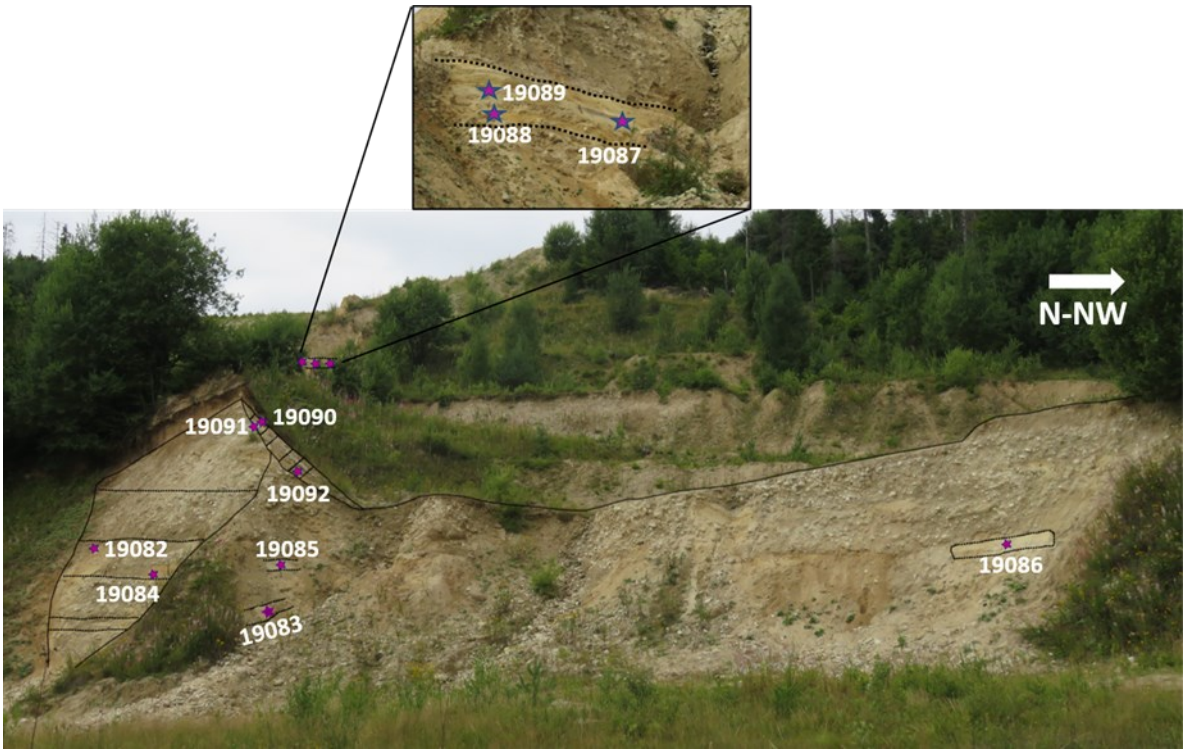

Figure 7. The Bee pit with the lower and upper gravel pits and the location where the samples were taken from (pink stars) and their corresponding number.

4.2 Sedimentology

4.2.1 Logging

The area of study is an abandoned gravel pit where two outcrops were selected to be cleaned and do the corresponding sedimentary description and stratigraphic characterisation. The first outcrop and main section is located in the lower area of the Bee pit, where most of the units were identified (Figure 7). The lithology, grain size, and basal contacts were documented in the log, drawn with 1:50 scale. The same procedure was done in the upper section, following the references from the chart for field description of Krüger & Kjær (1999) and the lithofacies code of Eyles et al. (1983), (modified by Helena Alexanderson and Per Möller 2017, pers.comm.) (Figure 8).

Lithofacies codes

Sorted sediment facies

1st code (grain size)

B	boulders
CoG	cobbles and gravel
G	gravel
SG / GS	sandy gravel / gravelly sand
S	sand
SiS / SSi	silty sand / sandy silt
Si	silt
CSi / SiC	clayey silt / silty clay
C	clay

2nd code (structure)

m	massive
mm	matrix-supported, massive
cm	clast-supported, massive

3rd code (structure)

(bi)	bimodal composition
(g)	graded
(ng)	normally graded
(ig)	inversely graded
(def)	deformation structures

Figure 8. Lithofacies code with the ones used to classify the Bee Pit units. Modified from Eyles et al. (1983).

4.2.2 Sampling for clast shape and Maximum particle size

The clast shape analysis, which has become a standardised method for reconstructing the transport history (Brook & Lukas 2012), consists of the collection of 50 clasts per unit. Six samples were taken from five different units composed of gravel. For each clast its three orthogonal axes were measured, with the longest (a), intermediate (b) and shortest (c) axes, which should be between 2 and 6 cm. Their roundness and texture, if they were broken or weathered, were also noted. The plotting of the three axes in the triangular diagrams following Sneed & Folk (1958), in the spreadsheets from Graham & Midgley (2000), is proved to be useful to display clast shape (Benn & Ballantyne 1993; Lukas et al. 2013). The ratios of a:b and a:c enable to identify if a clast has a blocky, where $a \approx b \approx c$, elongated, where $a >> b \approx c$ and slabby shape with $a \approx b > c$ (Figure 9) (Benn 2004; Lukas et al. 2013). It has been shown that the C_{40}-index, the ratio of clasts within a sample of $c:a \leq 0.4$, is effective to identify blocky from elongated and platy clasts. The maximum particle size was done by measuring the ten biggest clasts in the identified layers. Nine measurements were taken for this analysis from the units that had clasts.

4.3 Luminescence dating

4.3.1 Sampling

The samples were extracted in PVC tubes which were hammered horizontally into the vertically exposed sediments (Figure 10A). For OSL, eleven samples were taken along with the water content for each one of them, collected in soil sample rings that fit 100 cm^3

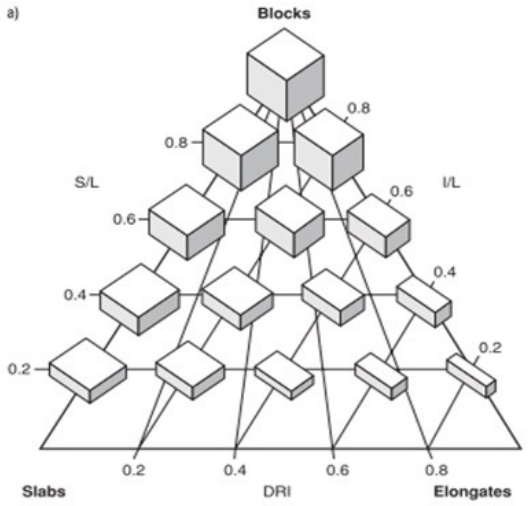

Figure 9. Schematic showing an equilateral triangular diagram, where the scaled used is the c:a (S/L) and b:a (I/L) axial ratios, taken from Evans & Benn (2014).

of material (Figure 10B). The samples were taken in both the upper and lower sections, from the different units identified in the pit, specifically from the ones composed by sand.

4.3.2 Preparation of the Samples

The OSL samples were prepared under subdued red light, avoiding any natural or white light which could cause weakening of the natural OSL signal. The water content measurements were done first, by weighing every metallic soil sample ring with sediment before they were saturated for around 24 hrs. Then they were weighed again and once more after being dried in the oven at 105°C for 24 hrs. The background samples, taken from the first 5 cm of the PVC tube, were weighed after being heated to 105°C for 24hrs first, to know the dry weight and then 450°C for 24 hrs to get rid of any organic matter. After being crushed, these background samples were mixed with bee's wax and cast into cups for gamma spectrometry at the Nordic laboratory for Luminescence Dating Risö, in Denmark (Figure 11A). The results of these values, along with the chosen water content, the equivalent dose and the coordinates of each sample are then used in an established spreadsheet that will be processed online by the Dose Rate Age Calculator (DRAC) (Durcan et al. 2015).

The remaining material in the tube is used to obtain sand-sized grains of quartz and K-feldspar. The size separation is done with wet sieving for fractions 63-355 µm (Figure 11B), where the 180-250 µm is the fraction used for the following chemistry stage. The extracted fraction is then treated with HCl (10%) to remove carbonates, H_2O_2 (10%) for organic materials, rinsed with deionized water between each step, and then dried in the oven at 30°C. Afterwards, the heavy liquid solution (LST fastfloat) with a density of

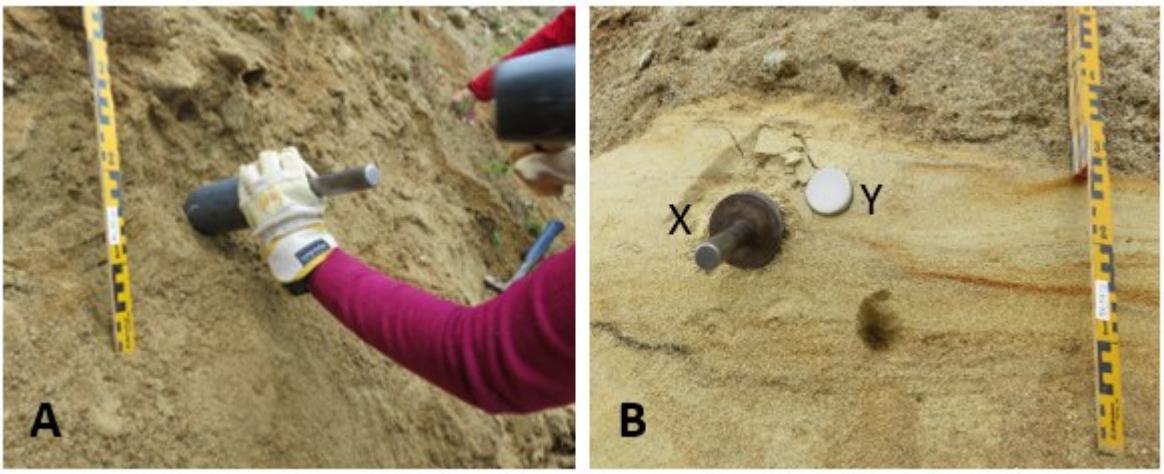

Figure 10. A) Hammering of the tubes in the Bee Pit to extract the samples. B) The two types of tubes used for sampling where X is the OSL tube and Y is the water content.

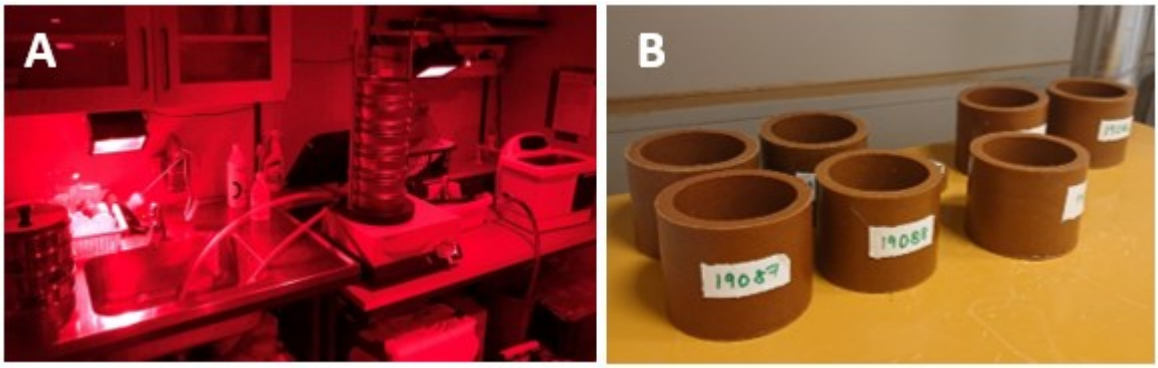

Figure 11. A) Sieving station in the Lund Luminescence Laboratory and B) the gamma cups made in the Risö Laboratory in Denmark.

2.62g/cm^3 is used to separate quartz from feldspar grains. The remaining quartz is treated with HF (40%) for 2x30 minutes and rinsed with deionized water. Afterwards it is treated again with HCl (10%), to remove any remaining fluorides. After rinsing, samples were dried and the dry sieving followed, which is done by hand with smaller sieves and only the size 180 µm. Then, if the sample contains magnetic grains these are separated from the quartz using a magnet and kept in separate tubes, making the sample ready to be measured in the machine.

To separate the extracted feldspar into potassium and sodium fractions, LST with 2.58g/cm^3 density is used. The potassium feldspar alone was etched with HF (10%) for 40 minutes, then treated again with HCl (10%), rinsed with deionised water and dried in the oven as well. The last steps to have the feldspar ready to be measured are the same as in quartz, with dry sieving by hand with the 180 µm fraction.

4.3.3 Measurements and Data Analysis

The luminescence measurements were made in Risö 'TL/OSL DA-20' readers at the Lund luminescence laboratory. A reader is composed of a light stimulator, detector, irradiator, and heater, where a blue light-emitting diode (LED) and an infrared (IR) LED were used as light stimulators (Bøtter-Jensen et al. 2000; Bøtter-Jensen et al. 2003). The light detector is a photon multiplier tube (PMT), the irradiation comes from a Beta irradiation source (^{90}Sr/^{90}Y) and when the measurement included heating above 200°C, nitrogen gas was used (Figure 12A). The samples were measured on aliquots where their size depended on the number of grains, which could be either large (8 mm) or small (2 mm) (Figure 12B). The aliquots used for quartz analysis were large and for feldspar small aliquots. The large aliquots have around 1000 grains and the small ones have around tens of grains. The feldspar aliquots from the Bee Pit samples had around 70 grains (Figure 12C). The machine measurements were done following the SAR protocol proposed by (Murray & Wintle 2000), and its subsequent quality control tests, which were programmed using the Risö sequence editor. The measurements done in the machine were carried out using three aliquots at a time per sample as an average, but it varied depending on the type of measurement and how long each one took.

Quartz Measurements

The first sequences were IR/B tests, done in order to check possible contamination of feldspar in the quartz samples. This was done by using both blue and IR LEDs, where the blue LED stimulates the quartz and

the infrared stimulates feldspar. The infrared is used before the blue because the feldspar signal needs to be cleared out beforehand, to ensure that the next measurement would be only the quartz signal. This was done in the following order first TL, then IR LED followed by blue LED.

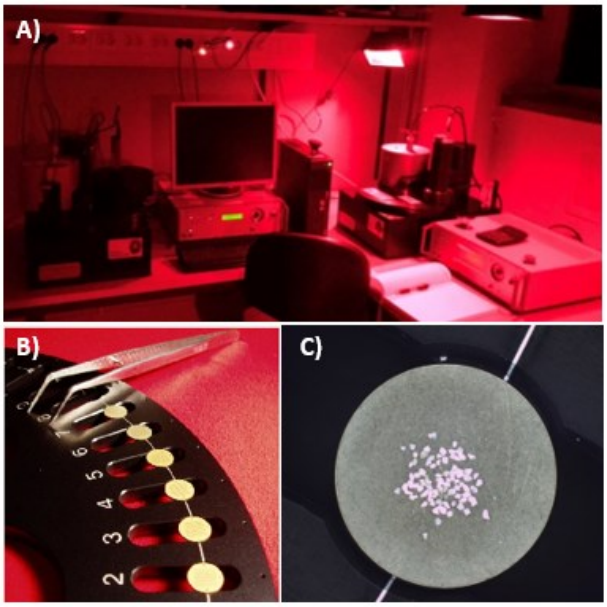

Figure 12. The Luminescence Laboratory: A) The two Risö 'TL/OSL DA-20' reader machines and B) the wheel with aliquots that goes inside the readers, taken from Analyst. v4.57 ed program. C) Small aliquot with feldspar grains used in one of the dose estimate sequences.

The next step was to do a pre-heat plateau test to determine the temperatures from which an average dose can be calculated. This was done with a series of combinations of temperatures, ranging from 180°C to 260°C for the first half of the cycle (preheat) and 160°C to 220°C in the second half (cutheat), with several full SAR protocol cycles. The recycling and recuperation tests are generally programmed in the fifth and sixth cycles of the sequence (Figure 13).

Then, the dose recovery test was performed to replicate the natural process of zeroing the OSL signal, by bleaching it with sunlight. Followed by giving a known dose and, with the SAR protocol, the dose was measured directly, as proposed in Wintle & Murray (2006). The selected samples that underwent this test were representative ones from the different sections located in the Bee Pit.

A first dose estimate measurement was then done on three aliquots per sample, for ten of the eleven collected samples. It targets to get the magnitude of the equivalent dose value by measuring first the natural signal and then measuring the dose after been given two doses in the second and third cycles of the SAR protocol.

The last two types of measurements that were done with quartz samples were pulsed (Ankjærgaard et al. 2010) and differential OSL (Jain et al. 2005). The pulsed stimulation takes into account that the luminescence signals from feldspar and quartz have different lifetimes with pulsed optical stimulation. Therefore, it is possible to discriminate between the two signals in a sample that presents a quartz-feldspar mixture by using this lifetime difference. This was done by following the proposed sequence settings in Ankjærgaard et al. (2010), to achieve a gated pulsed OSL using on and off- time settings each of 50 μs (i.e. a pulse period of 100 μs). This was tested on two different sequences, where the first one used nine aliquots of the sample 19082 measured with three different settings in the temperatures. The second pulsed OSL sequence was done with the same sample, using three aliquots and adding a preheat after the sample was given a dose.

Lastly, the SAR-protocol for OSL dating of quartz relies on a strong fast component of the OSL signal, but when the medium and slow components are quite significant, they can lead to erroneous dose estimates (Jain et al. 2005). Thus, a dose estimation method based on the OSL fast component alone was developed and in Jain et al. (2005), the possibility of depleting the fast component preferentially using IR stimulation was proposed. The result is a SAR protocol based on IR depletion of the fast component (Figure 14). This recommended protocol for differential OSL was tested on three samples with a sequence that repeats the whole cycle with three increasing doses (64, 128 and 192 Gy), then zero dose and a repeated dose.

Feldspar Measurements

Taking into account that IRSL on feldspar has been proved useful in areas where quartz OSL is found problematic, due to erosion of the sediment from bedrock, nearby deposition or when there are inclusions of feldspar (Lawson et al. 2012), the feldspar grains were also measured. This was done with different settings in the OSL machine filters than the ones used for quartz, which is the UV filter. Therefore, the UV filter was changed for the blue filter when using feldspar.

The first measurements done on feldspar were measurements of equivalent dose (D_e) on the representative samples, to estimate the correct set of laboratory doses that would be in the range of the sample's natural dose. A correct estimation means that the obtained dose of the samples should be neither over- nor underestimated of the given doses for both IRSL (at 50°C) and post IRSL (225°C) (Figure 15). The guideline for the amount of D_e measurements that each sample needed was twelve, which also depends on the spread of doses. This was done with a wide range of settings employing varying doses, that depended on the obtained doses from the eleven samples.

↓ ↓ ↓	Samples	Run 1	Run 2	Run 3	Run 4	Run 5	Run 6
Set 1	1-15		Beta 300s	Beta 800s	Beta 1500s	Beta 0s	Beta 300s
Set 2	1-3	TL 180°C, 5.00°C/s, 250Pts., P	TL 180°C, 5.00°C/s, 250Pts., P	TL 180°C, 5.00°C/s, 250Pts., P	TL 180°C, 5.00°C/s, 250Pts., P	TL 180°C, 5.00°C/s, 250Pts., P	TL 180°C, 5.00°C/s, 250Pts., P
Set 3	4-6	TL 200°C, 5.00°C/s, 250Pts., P	TL 200°C, 5.00°C/s, 250Pts., P	TL 200°C, 5.00°C/s, 250Pts., P	TL 200°C, 5.00°C/s, 250Pts., P	TL 200°C, 5.00°C/s, 250Pts., P	TL 200°C, 5.00°C/s, 250Pts., P
Set 4	7-9	TL 220°C, 5.00°C/s, 250Pts., P	TL 220°C, 5.00°C/s, 250Pts., P	TL 220°C, 5.00°C/s, 250Pts., P	TL 220°C, 5.00°C/s, 250Pts., P	TL 220°C, 5.00°C/s, 250Pts., P	TL 220°C, 5.00°C/s, 250Pts., P
Set 5	10-12	TL 240°C, 5.00°C/s, 250Pts., P	TL 240°C, 5.00°C/s, 250Pts., P	TL 240°C, 5.00°C/s, 250Pts., P	TL 240°C, 5.00°C/s, 250Pts., P	TL 240°C, 5.00°C/s, 250Pts., P	TL 240°C, 5.00°C/s, 250Pts., P
Set 6	13-15	TL 260°C, 5.00°C/s, 250Pts., P	TL 260°C, 5.00°C/s, 250Pts., P	TL 260°C, 5.00°C/s, 250Pts., P	TL 260°C, 5.00°C/s, 250Pts., P	TL 260°C, 5.00°C/s, 250Pts., P	TL 260°C, 5.00°C/s, 250Pts., P
Set 7	1-15	OSL 125°C IR LEDs;100.0 s;5	OSL 125°C IR LEDs;100.0 s;5	OSL 125°C IR LEDs;100.0 s;5	OSL 125°C IR LEDs;100.0 s;5	OSL 125°C IR LEDs;100.0 s;5	OSL 125°C IR LEDs;100.0 s;5
Set 8	1-15	OSL 125°C Blue LEDs;40.0 s;	OSL 125°C Blue LEDs;40.0 s;	OSL 125°C Blue LEDs;40.0 s;	OSL 125°C Blue LEDs;40.0 s;	OSL 125°C Blue LEDs;40.0 s;	OSL 125°C Blue LEDs;40.0 s;
Set 9	1-15	Beta 100s	Beta 100s	Beta 100s	Beta 100s	Beta 100s	Beta 100s
Set 10	1-3	TL 160°C, 5.00°C/s, 250Pts., P	TL 160°C, 5.00°C/s, 250Pts., P	TL 160°C, 5.00°C/s, 250Pts., P	TL 160°C, 5.00°C/s, 250Pts., P	TL 160°C, 5.00°C/s, 250Pts., P	TL 160°C, 5.00°C/s, 250Pts., P
Set 11	4-6	TL 160°C, 5.00°C/s, 250Pts., P	TL 160°C, 5.00°C/s, 250Pts., P	TL 160°C, 5.00°C/s, 250Pts., P	TL 160°C, 5.00°C/s, 250Pts., P	TL 160°C, 5.00°C/s, 250Pts., P	TL 160°C, 5.00°C/s, 250Pts., P
Set 12	7-9	TL 180°C, 5.00°C/s, 250Pts., P	TL 180°C, 5.00°C/s, 250Pts., P	TL 180°C, 5.00°C/s, 250Pts., P	TL 180°C, 5.00°C/s, 250Pts., P	TL 180°C, 5.00°C/s, 250Pts., P	TL 180°C, 5.00°C/s, 250Pts., P
Set 13	10-12	TL 200°C, 5.00°C/s, 250Pts., P	TL 200°C, 5.00°C/s, 250Pts., P	TL 200°C, 5.00°C/s, 250Pts., P	TL 200°C, 5.00°C/s, 250Pts., P	TL 200°C, 5.00°C/s, 250Pts., P	TL 200°C, 5.00°C/s, 250Pts., P
Set 14	13-15	TL 220°C, 5.00°C/s, 250Pts., P	TL 220°C, 5.00°C/s, 250Pts., P	TL 220°C, 5.00°C/s, 250Pts., P	TL 220°C, 5.00°C/s, 250Pts., P	TL 220°C, 5.00°C/s, 250Pts., P	TL 220°C, 5.00°C/s, 250Pts., P
Set 15	1-15	OSL 125°C IR LEDs;100.0 s;5	OSL 125°C IR LEDs;100.0 s;5	OSL 125°C IR LEDs;100.0 s;5	OSL 125°C IR LEDs;100.0 s;5	OSL 125°C IR LEDs;100.0 s;5	OSL 125°C IR LEDs;100.0 s;5
Set 16	1-15	OSL 125°C Blue LEDs;40.0 s;	OSL 125°C Blue LEDs;40.0 s;	OSL 125°C Blue LEDs;40.0 s;	OSL 125°C Blue LEDs;40.0 s;	OSL 125°C Blue LEDs;40.0 s;	OSL 125°C Blue LEDs;40.0 s;
Set 17	1-15	Illum Blue LEDs (90.0 %) for 4	Illum Blue LEDs (90.0 %) for 4	Illum Blue LEDs (90.0 %) for 4	Illum Blue LEDs (90.0 %) for 4	Illum Blue LEDs (90.0 %) for 4	Illum Blue LEDs (90.0 %) for 4

Figure 13. The sequence used to test a pre-heat plateau with various combinations of temperatures, the ones in the first half always higher than the ones in the second half. In cycle 5 (run 5) of the sequence the first dose is zero, indicating the recuperation test, and in the sixth cycle, where the first given dose is repeated, indicates the recycling test.

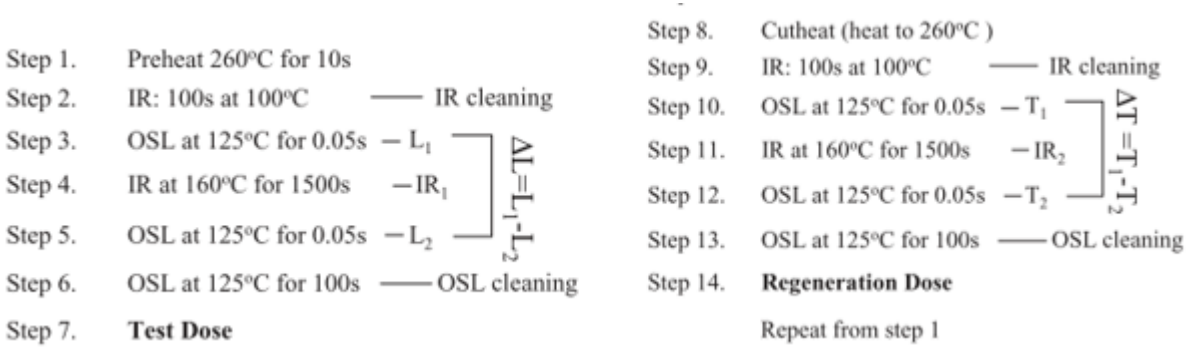

Figure 14. Diagram of the quartz differential-OSL SAR dose estimation method, as proposed by Jain et al. (2005).

Along with these previously mentioned measurements, the anomalous fading was measured using the same aliquots. Given that the fading measures the loss of signal over time, the aliquots would be given a dose and measured after having a pause, at the end of the D_e sequences. Likewise, after the first fading measurement was done, the aliquots were given a dose once more and set aside for about one week before they were measured for a second time. Following this pattern, on average each sample had three aliquots measured with at least four measurements, where each one is represented by a point in the fading graph. The L_x/T_x in the graph represents the ratio of the laboratory dose given to the aliquots at the end of the sequences and the test dose signals read after the delay. The calculation of the g-values was done in the Analyst v4.57 program.

The other two tests that were done on the feldspar samples were the dose recovery and residual. As it was previously explained, these two measurements cope with measuring the samples after being exposed to light or bleached, then they are given a laboratory dose that undergoes a full SAR protocol sequence measurement. Consequently, ten aliquots from five representative samples were made and exposed to sunlight by leaving them indoors on a window sill for about a week. Later, half of the aliquots were used to measure dose recovery and the other half for residual.

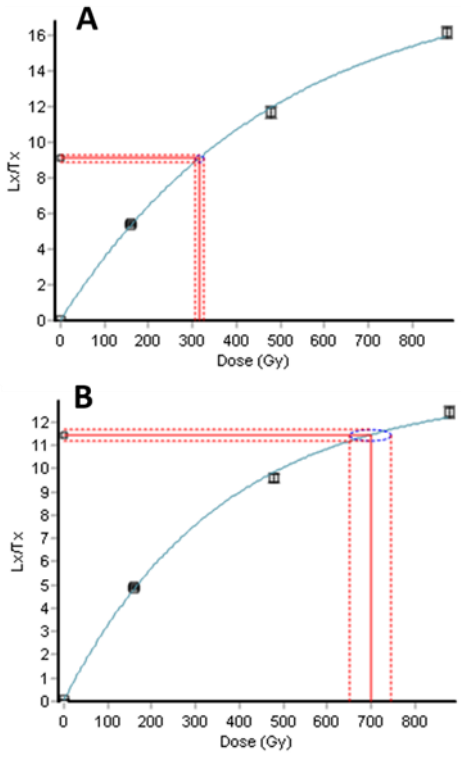

Figure 15. Example of growth curve and dose estimates for sample 19085, for both IRSL 50° C (A) and post-IR IRSL 225°C (B) showing the measured dose within the given regeneration doses 160, 479 and 878 Gy. The D_e was determined to 328 Gy and 708 Gy, respectively.

4.3.4 Age estimation

After doing all the needed measurements of the samples, along with the obtained results, the ages are calculated three times, and each version is dependent on different water content values, previously weighed in the laboratory (Table 2). The first one is taken from the value when the sediments are saturated, secondly when the sediments have been dried and then a value that is assumed based on how it is believed the groundwater level and geology have been affecting the sampled sediments. For the Bee Pit samples, they were given the saturated water content percentage depending on the vertical distribution of the outcrop. The five samples located towards the bottom of the lower section were given an 80-90% of saturation and 20-10% of field water content, assuming that they have had the closest proximity to the groundwater level. The three samples located at the top of the lower section had an assumed value of 70% of saturated and 30% field water content. The remaining three samples, located in the upper section of the Bee Pit were given 40% of saturation and 60% field water content since they are further away from the groundwater level.

Table 2. The water content values used for the age calculation, per sample.

Sample No.	Field Water Content (%)	Saturated Water Content (%)	Chosen Water Content (%)
19082	11	31	27
19083	15	25	24
19084	7	22	19
19085	13	25	23
19086	21	27	26
19087	24	35	29
19088	23	30	26
19089	15	27	20
19090	15	35	29
19091	17	31	27
19092	32	38	36

Once all the samples have their corresponding results, given the fact that they were measured on feldspar it is needed to correct them for fading, using the previously obtained g-values. This process is done using the luminescence option in R-studio program with a formula that includes the age, g-value, the error for both and the prompt. The prompt value is taken from the dose estimates sequences and represents the time in between when the aliquot was irradiated and immediately measured. This procedure helps to correct the ages for fading, since without correction the ages would seem younger. Another feature that helps assess the age estimation is the saturation value of the samples, whether the sediments are or are not saturated based on the signal measured in the dose estimation. According to Wintle & Murray (2006) when having high natural doses, it is advised to ensure that the $D_e < 2D_0$ to

avoid saturation problems and uncertainties on the D_e values.

5 Results

The obtained results from the laboratory analysis and luminescence dating are broadly divided into sedimentology and luminescence. Each section deals with the different samples collected during the fieldwork.

5.1 Sedimentology

The description of units will be explained in two separate sections of the Bee Pit, lower and upper. Both sections are located towards the western side of the Biely Váh river. The lower one is around 45 m wide and 13.6 m in height, while the upper one is around 6 m high. Among the two sections they comprise 13 units and the two sections are separated vertically by around 20 m. The log presents both upper and lower sections of the Bee Pit, with all the identified units (Figure 16).

5.1.1 Bee Pit Lower Section

Unit 1A

The thickness of the unit is 1.80 m, the lower boundary is covered by slump and could not be identified. The unit is composed of massive gravel with clasts that range from cobbles to boulders (~32 cm as maximum size). The clasts present sizes ~8 cm or less and have a high degree of weathering (80-90% of the clasts), making them very brittle, with a granite lithology. This unit is classified as massive, matrix-supported cobbles and gravels (CoGmm) with a bimodal nature.

Unit 1B

It is around 20 cm thick and has a sharp boundary with the underlying unit 1A. It is a massive unit composed of sandy-silt (Figure 17A), with a gravel lens towards the centre of the outcrop and it is classified as massive sandy silt (SSim).

Unit 2

The thickness is 1.60 m and it presents a sharp boundary to the underlying unit. It is composed of massive coarse sand with matrix supported cobbles and boulders and it is described as bimodal. The matrix fines upwards from the very coarse sand located at the bottom of the layer. The boulders are composed of granite with a high degree of weathering making them very brittle. Around 80-90% of the clasts are weathered. In some areas the sediment is clast supported, but otherwise it is matrix supported. The sediment is classified as massive, normally graded, matrix-supported cobbles and gravels CoGmm(ng).

Unit 3

This unit is 1.50 m thick, with a sharp underlying boundary, it is massive and is composed of coarse to very coarse sand, with laminations that show evidence of oxidation. Given the height from the floor level, this unit was described only at the sides of the exposure, therefore the lens of gravel and cobbles towards the centre of the layer was unreachable and could not be described further. From the bottom of the unit, it generally grades to coarse sand, with a thin layer (~8 cm) of silt towards the top. On the N-NW side of the layer, in a small area there seems to be planar stratification, followed by vague crossbedding (Figure 17B). It was not possible to follow this level to the rest of the layer because it was inaccessible. Towards the side of the outcrop, in the gully there is a ~60 cm section of sand that fines upward to silt to the top. The whole unit is classified broadly as massive, normally graded silty sand (SiSm(ng)) (Figure 17A).

Unit 4

This unit is around 4 m thick; it is located very high up in the outcrop and its inaccessibility made it harder to describe. It is defined as a coarse grained, sandy and gravelly, massive unit with cobbles that is fining upwards. It is classified as massive, matrix-supported, normally graded cobbles and gravels (CoGmm(ng)). Towards the side of the main outcrop, two boulders were found measuring 180 cm and 230 cm, bigger than any of the others, and in extremely weathered condition (Figure 17C).

Unit 5

The thickness of the unit is 60 cm, it is mainly composed of massive sand which grades upwards from very coarse sand to very fine sand and silt. There are gravel lenses with some oxidized and possibly laminae with black manganese precipitation towards the bottom of the layer. The boundary with the underlying unit is sharp. The unit is classified as massive, normally graded sand (Sm(ng)) (Figure 17D).

Unit 6

This unit is mainly composed of gravel and has a thickness of 45 cm with a sharp boundary to the underlying unit. The description was done briefly due to the cover of slump, proximity to the edge of the outcrop and height, making this layer unapproachable (Figure 17E) and it is classified as massive gravel (Gm).

Unit 7

The thickness of this layer is 30 cm and it is a massive unit, composed of silty fine sand. It presents some clasts towards the base, where the boundary with the underlying unit is sharp and slightly uneven and it is classified as massive silty sand (SiSm).

Unit 8

This unit has a thickness of 80 cm, it is primarily composed of massive coarse sand and gravel with a size of clasts that ranges between cobbles and boulders. The clasts are made up of granite and they are found more to the E than to the W of the layer. The sediment is classified as massive sandy gravel (SGm).

Unit 9

Unit 9 is 57 cm in thickness; it is massive silty sand that ranges from fine to medium, with some coarse sand lenses (Figure 17F). Towards the base there are some weathered clasts, which are partly clast supported. The boundary between the underlying unit is sharp but a little uneven and the sediment is classified as massive silty sand (SiSm).

Unit 10

The thickness of this layer is 1.80 m, there are cobbles and boulders with a matrix composed of medium to coarse sand. The number of clasts is higher than in the underlying units. There is matrix between the clasts, but they are also partly in contact. The underlying boundary is very uneven but still sharp and it is classified as massive, clast-supported cobbles and gravel (CoGcm).

Interpretation

The lower section of the Bee Pit has several different depositional stages, which relate to environments with clear energy differences, since there is an evident variation in the grain sizes, with cobbles and gravels, fine sand and silt units overlying each other. The deposition of units 1A, 2, 4, 6, 8 and 10 needed a very high energy component which allowed that amount of coarse material and boulders to be deposited. Likewise, these units have the thickest layers which also implies an abundant availability of material at the time of deposition. This is especially the case for unit 4, which is the thickest and contains the biggest boulders of the whole Bee Pit. This could lead to assuming the occurrence of big sudden events that would be capable of forming such thick and coarse layers. Considering the high energy that would be needed in these events, and the massive coarse-grained deposits, it could be possible to relate these units to massive flooding or debris flow events.

Furthermore, the units 1B, 3, 5, 7 and 9 are dominantly composed of sand and silty sand, which indicate a change in the depositional environment compared to the coarser units. For these units to form there must have been a reduction in the energy of transport. The sands are dominantly massive, indicating that the depositional process could have occurred rapidly. In unit 3 there are indications of normal grading from very coarse to coarse sand at the bottom up to fine sand/silt in the top. Also, there are some lenses among the sand layers of both silt and coarser material indicating a possible fluvial component in the deposition.

5.1.2 Bee Pit Upper Section

Unit 11

The thickness of this unit is estimated at around 1.6 m thick since the lower boundary was still covered by slump (Figure 16). It presents an uneven, sharp boundary with the overlying unit of sand. The matrix is composed of coarse sand, with very weathered clasts that range from cobbles to boulders, which are granite in lithology. The sediment is classified as massive, matrix-supported cobbles and gravel (CoGmm) with a bimodal nature (Figure 17G).

Unit 12

Unit 12 is 2 m thick with two layers that are fining upwards from very coarse - coarse sand to silt, towards the middle of the layer. Overlying this is medium sand with some gravel layers, and then it is grading again to very fine – silty sand in the top. It has a sharp boundary with the overlying unit. In the middle of the sand unit, where the silt changes to sand, there also is an uneven boundary. Towards the centre of the unit there is a silty lens/clast, it has an apparent planar stratification and is surrounded by granite clasts (Figure 17H). Towards the top of the layer there is a silty/clayey level, which seems to have a structure of lines that become successively more vertical closer to the silt clast. Overlying the lens is a fine, undeformed sand. The unit is dominated by massive, normally graded sand (Sm (ng)), with minor components of massive, silty sand (SiSm) towards the top (Figure 16).

Unit 13

The thickness of this unit is also estimated at 2 m, composed of a massive gravel matrix with clasts that range from cobbles to boulders in size. Clasts are of granite lithology, very weathered and brittle. The unit is classified as massive, matrix-supported cobbles and gravel (CoGmm).

Interpretation

The interpretation for unit 11 and unit 13 is similar to the previously described one for the coarser units from the lower section. Their deposition needs a high energy way of transport to allow the abundant cobbles and boulders to be present in the units. For unit 12 the silt lens suggests a drastic change in the energy level. The localized structures imply a possible deformation during deposition since the overlying layer is horizontal and not affected by the deformation. Overall, this unit has a clear change in the depositional process in relation to the underlying and overlying units, and unlike the units of the lower section, the found structures imply the calm period was longer, allowing them to form.

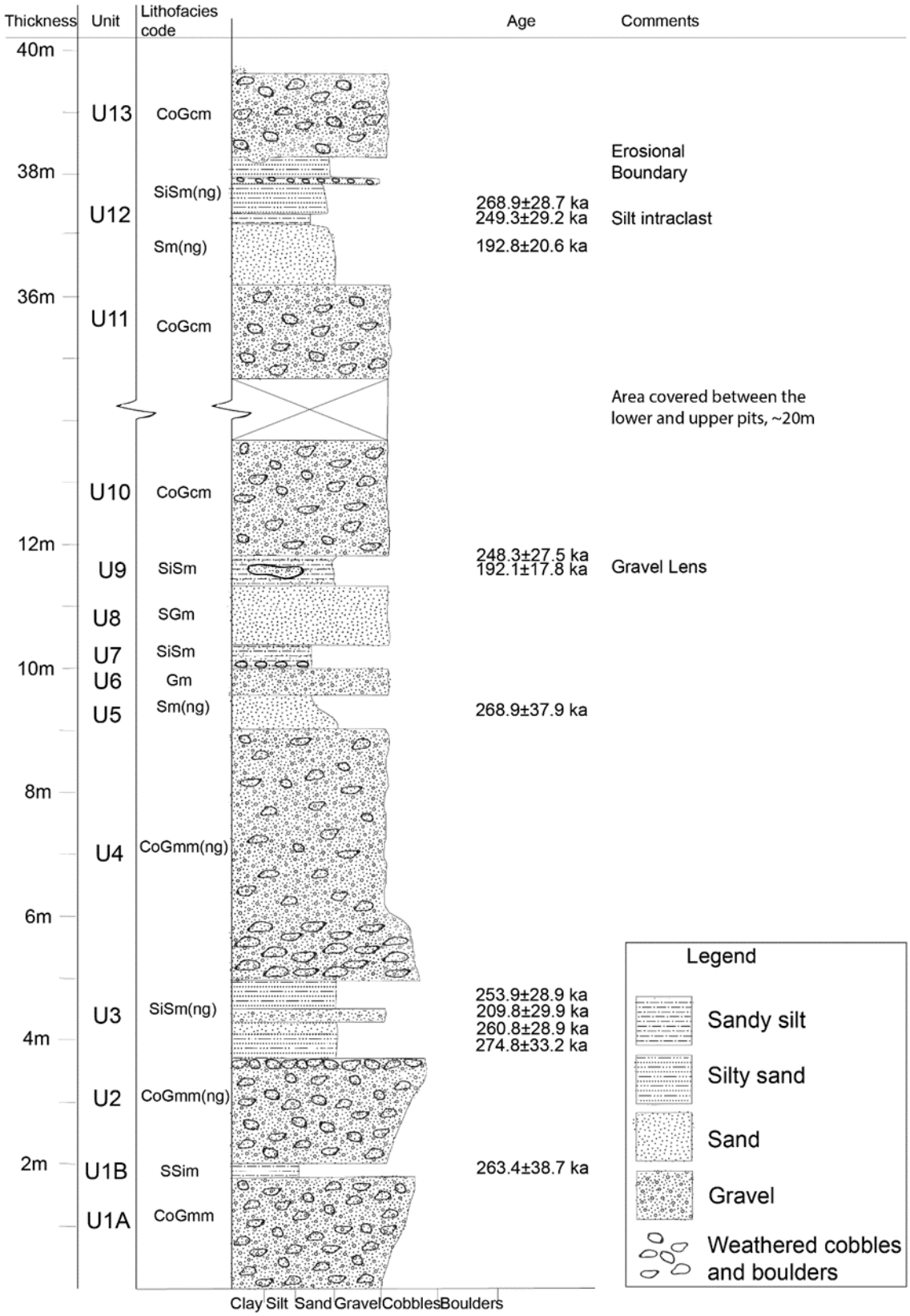

Figure 16. General log depicting all the Bee Pit units with the ages from the collected samples. The lithofacies code legend is found in Figure 8.

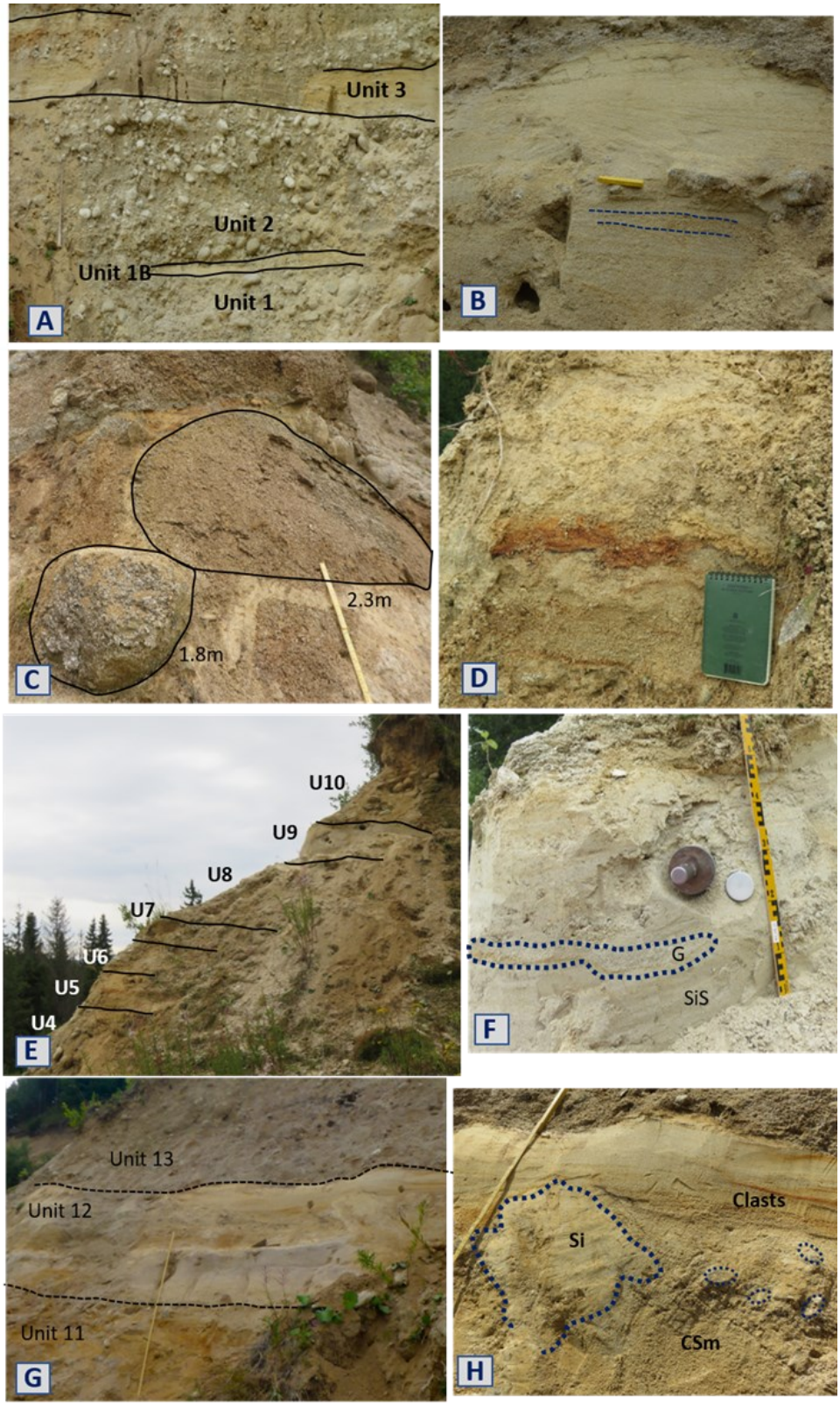

Figure 17. Photos taken from the different units in the Bee Pit. A) Outcrop from the lower section showing the bottom three units. B) Detail from unit 3 depicting stratification C) The Two biggest boulders from all the area, present a very high degree of weathering and are found in unit 4. D) Detail of the possible manganese and oxidation laminae from unit 5. E) Disposition in the outcrop of the top units of the lower section. F) Detail of the gravel lens found in unit 9. G) Disposition of the units in the upper section. H) Detail from unit 12 showing the silt lens with granite clasts to the right and the local erosional boundary with the overlying unit.

5.1.3 Clast Shape and Maximum Particle Size

Clast shape analysis

For the clast shape analysis six samples were taken from the units where clasts > 2cm were abundant, resulting in two samples for unit 1A and one sample each for unit 2, unit 4, unit 11 and unit 13. The clasts of both samples from Unit 1A are overall blocky to slightly platy (Figure 18a and b). Clasts within the sample from unit 2 have a blocky shape (Figure 18c) and a similar result was obtained for the sample from unit 4 (Figure 18d), unit 11 (Figure 18e) as well as unit 13 (Figure 18f). The results for roundness and angularity have some degree of variation between samples (Figure 19), but clasts were generally between subrounded and subangular. Additionally, two co-variance plots were made, using the C_{40} against both the RWR and RA values (Figure 20).

Maximum particle size (MPS)

Nine MPS measurements were taken mainly from the lower section of the Bee Pit, with one sample from unit 1A, one from unit 2 and five samples from unit 4. In the upper section, two samples were taken from units 11 and 13. Most of the samples were taken from unit 4 given that it is one of the thickest layers and accessible to measure the cobbles and boulders through the gully. The range of values for unit 1A and unit 2 was quite similar (13-29 cm). For unit 4 the values have a wider range from 12-60 cm, with two exceptionally big boulders of 180 cm and 230 cm (Figure 16C). In units 11 and 13 the range of sizes was quite similar to the units from the lower section (16-31 cm).

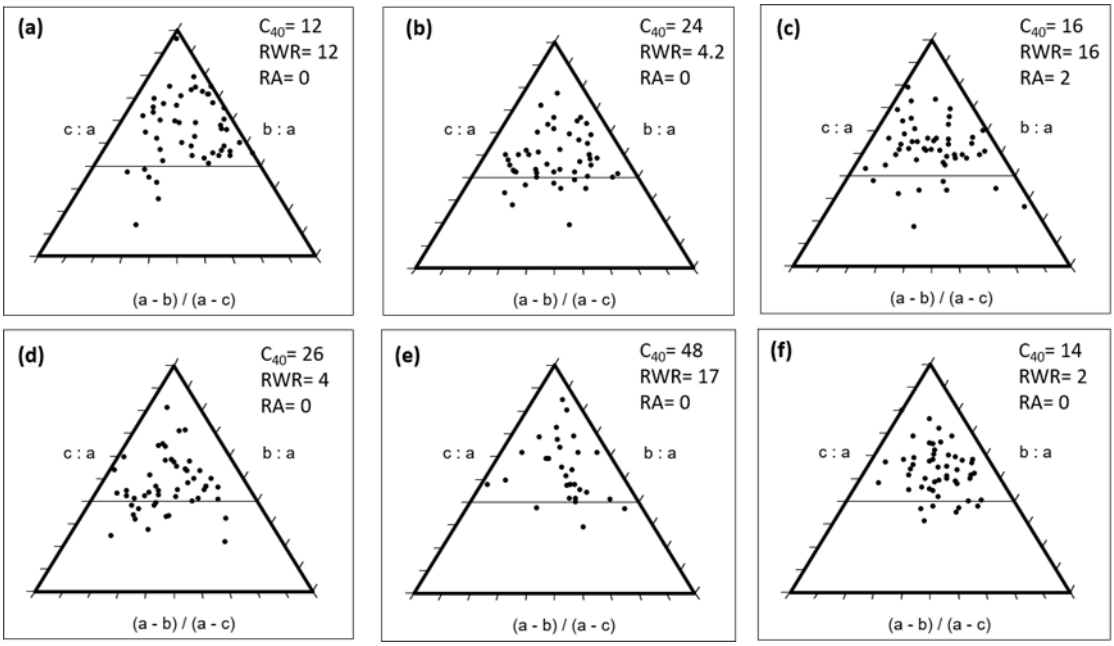

Figure 18. Clast shape data in triangular diagrams from Sneed & Folk (1958), plotted with the spreadsheet from Graham & Midgley (2000), for the samples taken from: a) Unit 1A sample A, b) unit 1A sample B, c) unit 2, d) unit 4, e) unit 11 and f) unit 13.

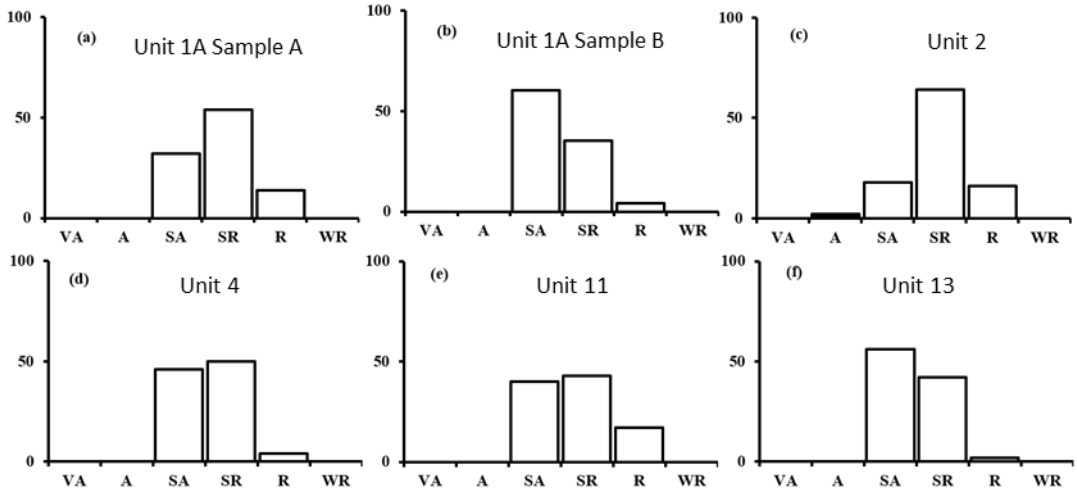

Figure 19. Roundness and angularity of the clasts plotted with the spreadsheet (Graham & Midgley 2000).

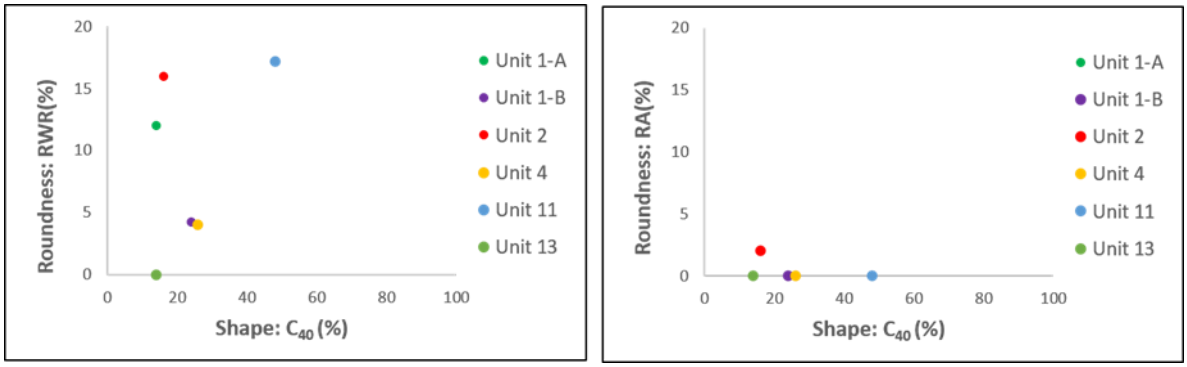

Figure 20. Covariance plots showing the C40 index plotted against: A) RWR and B) RA for the six samples collected for clast shape analysis.

5.2 Luminescence dating

The outcome of the sampling process for OSL were seven samples from the lower section, in the main outcrop, one from the area to the NW and three from the upper section of the Bee Pit (Figure 7). For each one of the eleven samples there was a soil sample ring for water content and background sample taken as well. The list of all the collected samples with their coordinates and corresponding unit can be found in Appendix B. To have a better understanding of various results obtained from the analysis of these samples their description is done for quartz and feldspar separately.

5.2.1 Measurements on Quartz

IR/B Test

As previously explained in 4.3.3, the first measurement done for Quartz was the IR/B test. From this test it was clear that the quartz grains were indeed contaminated with feldspar since the percentage for the IR/B ratio was evidently higher than 10%, ranging from 16% to 46%, with sample 19088 as an exception with much higher values (Table 3).

Table 3. The infrared to blue ratios from the IR/B test for all the samples of the Bee Pit.

Sample No.	IR/B Ratio	Sample No.	IR/B Ratio	Sample No.	IR/B Ratio
19082	31%	19086	22%	19090	23%
19082	19%	19086	26%	19090	35%
19082	34%	19086	29%	19090	30%
19083	24%	19087	26%	19091	30%
19083	26%	19087	26%	19091	26%
19083	28%	19087	30%	19091	46%
19084	27%	19088	315%	19092	40%
19084	16%	19088	197%	19092	33%
19084	25%	19088	924%	19092	23%
19085	22%	19089	30%		
19085	18%	19089	31%		
19085	33%	19089	19%		

Pre-heat Plateau Test (PHP)

The PHP test was done firstly on the representative sample 19082, this one was chosen as representative because it had enough material and it belongs to unit 3, which is one of the thickest sand units in the lower section. Similarly, this allows it to be measured several times and do all the tests for several trials, before applying it on the rest of the samples. The results of the PHP test show no evident plateau (Figure 21A). There could be a trend, taking into account the mean of the doses, at 150 Gy, but it is not reliable.

Recycling and Recuperation

The recuperation measurements varied depending on the sequence that was being measured, but in general the values were near to the accepted < 5%, ranging between 4 - 10%. Nevertheless, most of the measurements had a recycling error, implying values of more than 10% from unity.

Dose Recovery

The dose recovery values from the quartz samples were analysed by using the dose recovery ratio. The comparison of the ratios should be around one (0.9-1.1) and are calculated by dividing the measured dose by the given dose (Table 4). These values were plotted against the temperatures and it showed that per aliquot only two temperatures gave ratios close to 1 (Figure 21B). From the first measurement the temperature 260°C was chosen to try on the rest of the samples because even though the ratio was not among the accepted range, it was the closest to it and the only temperature where both points in the graph were close to each other. The following measurements done on the three other samples did not yield better results, most of the sample had ratios that were not within the accepted parameters. Generally, the ratios were smaller than one, implying that the measured doses underestimated the given dose. A ratio greater than one reflects a bigger measured dose in comparison to the given one.

Table 4. Dose recovery ratios for the measured samples for quartz.

Sample No.	Mean Dose Recovery Ratio (Gy)	Error (Gy)
19082	0.80	0.19
19084	0.65	0.11
19086	1.14	0.27
19089	0.53	0.09

Dose Estimate, Differential and Pulsed OSL

In the end, the equivalent dose was not determined for all the quartz samples because their data indicated that they were not giving acceptable results. Nevertheless, dose estimates were made for three samples (Table 5).

Since the large apparent feldspar contamination (high IR/B ratio, Table 3), the Pulsed OSL was used for the dose estimation (Ankjærgaard et al. 2010) and differential OSL was also tried (Jain et al. 2005). Unfortunately, there was no evident improvement of the measurements neither for pulsed OSL or for differential dose. The dose estimates were not improved and there were problems with test dose errors. Neither was the aim to isolate the fast component of quartz signal (Figure 22) with differential OSL reached, which is not good for dating. So, the conclusion was that the quartz samples of the Bee Pit are poorly behaved ones and therefore the analysis shifted the focus to feldspar.

5.2.2 Measurements in Feldspar

Dose Recovery and Residual dose

The measurements of dose recovery and residual were done with the previously bleached aliquots. The results of the dose recovery were analysed in a spreadsheet to calculate their ratio. The best ratios (the ones closer to one) are the ones obtained for the post IR-IRSL 225°C ($pIRIR_{225}$) (Table 6), though most of them are in the lower 10% of the accepted range. In the case of the residual dose the six measured samples had a small amount of signal left in the IRSL 50°C (IR_{50}), with doses that range between 2.56-2.96 Gy. Meanwhile for $pIRIR_{225}$ the residual doses had values between 15.05-17.53 Gy.

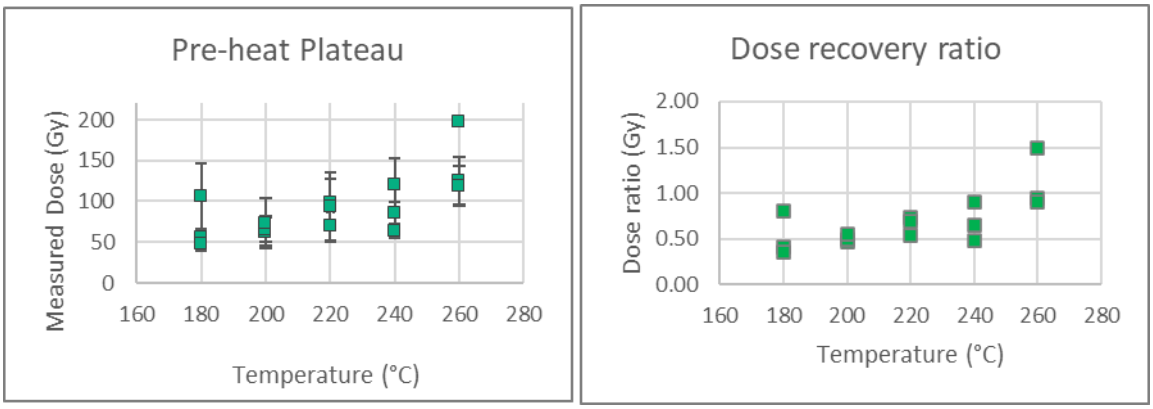

Figure 21. A) The PHP test from sample 19082. B) Dose recovery ratio plotted against temperature for sample 19082.

Table 5. The equivalent dose values for the samples measured with standard SAR protocol, for quartz with three aliquots each.

Sample	Mean Dose (Gy)	Error (Gy)	Sample	Mean Dose (Gy)	Error (Gy)
19083	143.42	26.94	19090	96.27	10.57
19084	159.635	40.74	19091	186.06	55.17
19085	103.29	20.97	19092	113.91	39.75

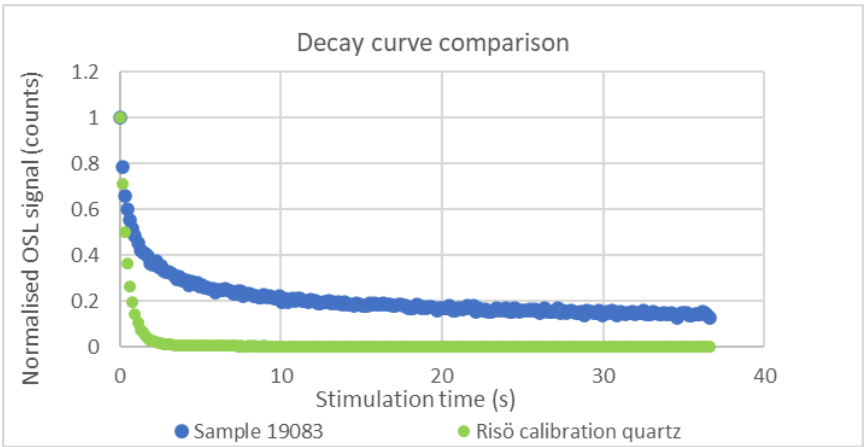

Figure 22. Decay curve comparison between calibration measurement of quartz and the dose estimate measurement for quartz from sample 19083, in the x-axis, is plotted the OSL signal (counts) and on the y-axis is the stimulation time (s). The slow decay of the curve of sample 19083 shows a signal that is not dominated by a fast component.

Table 6. Dose recovery ratios and residual doses for IR_{50} and $pIRIR_{225}$ measured on the same six samples, taken as representative for the rest of the samples from the area.

	IRSL 50°				Post IR-IRSL 225°C			
Sample No.	**Dose recovery ratio**	**Dose recovery error**	**Residual**	**Error**	**Dose recovery ratio**	**Dose recovery error**	**Residual**	**Error**
19082	0.89	0.03	2.73	0.17	0.92	0.03	16.09	0.12
19083	0.84	0.03	2.56	0.07	0.89	0.03	15.05	0.10
19086	0.86	0.03	2.96	0.11	0.87	0.03	17.32	0.10
19087	0.84	0.03	2.64	0.11	0.90	0.03	17.53.	0.10
19091	0.84	0.03	2.73	0.08	0.92	0.03	15.61	0.50
19092	0.88	0.03	-	-	0.91	0.03	-	-

Dose Estimate

The results obtained from the first dose estimates in the feldspar showed an improvement, compared to quartz, by showing that the curve had a rapid decay. The first couple of measurements were mostly overestimated implying that the dose of the grains was higher than the doses that were given to them (around 65, 130 and 194 Gy) for both IR_{50} and $pIRIR_{225}$. These were done on all the samples and all of them showed similar results. The correct estimation of the dose was reached by having a few more attempts with increased values for the three regeneration doses given. Dose estimate measurements were made on at least twelve aliquots, to have a sufficient amount of measurements. The final obtained doses for each sample are summarised in Table 8A.

Anomalous Fading

Fading measurements were done on all the eleven samples several times until they had a sufficient amount of points in the graph with different spaces of time in between. These periods for which the measurements were repeated could vary between a week or in some cases around a month. The obtained graphs for the fading look like Figure 23, where all samples show at least four measurement points. IR_{50} has the biggest values ranging between 9.83 and 1.66 (%/decade), meanwhile, for the $pIRIR_{225}$ they were smaller with 2.84-0.09 (%/decade) (Table 8B).

5.2.3 Dose Rate and Age Calculation

The concentrations of Uranium, Thorium and Potassium, depicted from gamma spectrometry are shown for each sample in Table 7. The results from these values are given with the age of the samples, along with their environmental dose, which is composed of the dose rate plus the cosmic radiation (Table 7). In addition to this, the results for saturation of the doses showed that all of the samples tested from IR_{50} were not saturated and most of them from $pIRIR_{225}$ were close to or at saturation. This is an expected result since $pIRIR_{225}$ has a higher signal than the IRSL 50°C. Nevertheless, all samples had some measurements that were not saturated, except for sample 19086 (Table 9).

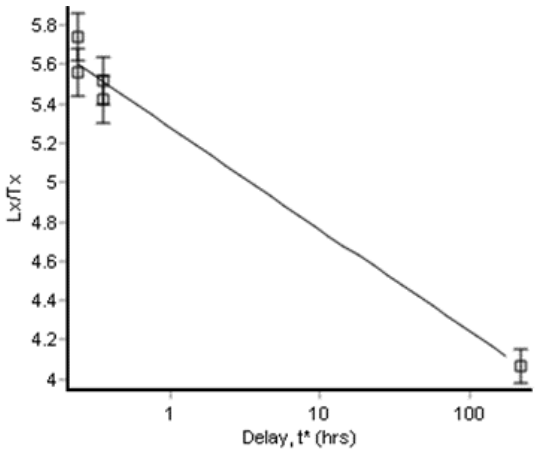

Figure 23. Fading graph where the loss of signal is shown by plotting the L_x/T_x against the delay in time. The x-axis is the time in hrs and the y-axis is the ratio of the laboratory signals with the test dose signals. The graph is made with the program Analyst from the Risö package (Duller 2018).

Table 7. Concentration of radioactive elements in the sampled sediment.

Sample No.	U (ppm)	U Error	Th (ppm)	Th Error	K %	K Error
19082	1.49	0.58	5.87	0.15	2.52	0.04
19083	0.960	0.450	6.550	0.130	2.420	0.050
19084	0.48	0.17	4.98	0.08	1.91	0.03
19085	0.92	0.54	5.11	0.14	2.23	0.04
19086	2.43	1.24	8.48	0.33	2.86	0.10
19087	1.22	0.42	6.96	0.12	1.99	0.04
19088	4.23	0.84	9.35	0.23	2.46	0.05
19089	1.04	0.21	5.6	0.08	2.52	0.03
19090	0.74	0.71	5.97	0.18	2.32	0.05
19091	2.08	0.39	8.79	0.11	2.59	0.03
19092	2.20	0.79	7.27	0.21	2.74	0.05

Table 8. A) Feldspar dose data with the unit, number of aliquots used/ total of measured, D_e and dose rate values. B) g-value, uncorrected and corrected for fading age.

A)

Sample No.	Unit	No. of aliquots	D_e (Gy)		Dose Rate
			IRSL at 50°C	Post-IR IRSL at 225°	
19082	Unit 3	12/21	426.4 ± 15.6	880.0 ± 87.8	3.326 ± 0.169
19083	Unit 1B	12/15	423.4 ± 16.6	970.2 ± 119.4	3.206 ± 0.164
19084	Unit 3	12/12	462.0 ± 21.5	955.1 ± 104.4	2.698 ± 0.146
19085	Unit 3	12/15	351.0 ± 12.2	792.9 ± 68.3	2.993 ± 0.164
19086	Unit 3	12/14	461.1 ± 18.1	1009.3 ± 106.2	3.869 ± 0.233
19087	Unit 12	12/15	403.2 ± 14.5	869.4 ± 76.5	2.929 ± 0.153
19088	Unit 12	12/15	363.6 ± 12.7	827.7 ± 74.0	4.025 ± 0.197
19089	Unit 12	12/12	414.6 ± 15.0	876.9 ± 89.6	3.411 ± 0.16
19090	Unit 9	12/12	420.2 ± 15.0	866.9 ± 77.9	3.074 ± 0.172
19091	Unit 9	12/15	402.6 ± 14.5	814.2 ± 73.8	3.696 ± 0.165
19092	Unit 5	12/21	559.8 ± 24.6	998.5 ± 108.7	3.528 ± 0.177

B)

Sample No.	g-value (%/decade)		Uncorrected age (ka)		Corrected age (ka)	
	IRSL at 50°C	Post-IR IRSL at 225°	IRSL at 50°C	Post-IR IRSL at 225°	IRSL at 50°C	Post-IR IRSL at 225°
19082	6.71 ±0.05	2.23 ± 0.30	125 ± 7.8	261 ± 29	278 ± 18	326 ± 38
19083	4.82 ± 0.71	1.56 ± 0.12	109 ± 7.2	263 ± 39	185 ± 28	308 ± 51
19084	9.83 ± 0.23	2.84 ± 0.18	129 ± 8.7	275 ± 33	624 ± 82	368 ± 46
19085	6.52 ± 0.08	1.66 ± 0.58	106 ± 6.8	254 ± 29	230 ± 16	300 ± 39
19086	1.66 ± 0.58	0.09 ± 0.10	99.9 ± 7.3	210 ± 30	117 ± 8.7	212 ± 29
19087	5.06 ± 0.28	1.48 ± 0.09	120 ± 7.6	269 ± 29	208 ± 16	311 ± 31
19088	5.85 ± 0.23	0.81 ± 0.56	80.9 ± 4.9	193 ± 21	156 ± 12	208 ± 27
19089	5.05 ± 0.02	1.99 ± 0.02	109 ± 6.6	249 ± 29	188 ± 11	304 ± 36
19090	5.71 ± 0.36	2.16 ± 0.09	115 ± 7.8	248 ± 28	219 ± 22	308 ± 31
19091	8.69 ± 1.06	0.37 ± 0.41	97.3 ± 5.7	192 ± 18	318 ± 185	199 ± 19
19092	5.26 ± 0.29	0.70 ± 0.43	132 ± 8.6	269 ± 38	236 ± 19	287 ± 39

*Table 9. Number of aliquots close to or at saturation (D_e>2*D_0) in both IRSL 50°C and PIRIRSL 225°C.*

	Sample	19082	19083	19084	19085	19086	19087	19088	19089	19090	19091	19092
IRSL 50°C	Non-Saturated	12/12	12/12	12/12	12/12	12/12	12/12	12/12	12/12	12/12	12/12	12/12
PIRIRSL 225°C	Saturated	11/12	11/12	10/12	11/12	12/12	10/12	11/12	10/12	9/12	8/12	10/12

6 Discussion

6.1 Sedimentology and Depositional Processes

The sedimentary properties of the 13 previously described units, clearly show a difference in the energy during the process of deposition for the coarse and finer layers. In the case of the coarser units, the big quantity of clasts that ranges from cobbles to boulders is indicative of high energy. Given the position of the outcrop and its proximity to the Tatra Mountains, sudden high energy events may occur as massive floodings or possibly as debris flow. Kotarba (2007) mentions in his studies that debris flows are quite common in high-mountain belts of European massifs.

Taking into account the six samples analysed for clast shape, it can be observed that clasts within all of them have a general blocky shape. Some variations were observed in their C_{40} indexes especially the sample from unit 11, which had the highest value, in comparison to the RWR, which yielded smaller variations (Figure 18). On account of the covariance plots allowing to distinguish the transport and depositional history of the clasts in an effective way (Benn & Ballantyne 1994), these were made with both the C_{40}-index vs. RWR as well as C_{40}-index with RA (Lukas et al. 2013) (Figure 19). Overall, they show that the transport history of the clasts most likely had an active transport component, given the low values of RA, in addition to the general blocky shape of the clasts, the higher values of RWR and medium C_{40} values. It is stated that, the clast shape depends on the process of transportation and lithology (Ballantyne 1982). Also, the active transport of clasts from the same lithology tends to have a compact, blocky shape, which displays a subglacial transport component (Benn & Evans 2010). As seen from the results (Figure 18), the majority of the clasts had a blocky shape, which is comparable to the results obtained in Graham & Midgley (2000). In their study, samples collected in the mountains of Scotland from moraine-mounds and fluvial deposits were also composed of granite and had as a result blocky shape in the triplots. Likewise, actively transported debris could have the balance between the processes of fracture and abrasion that could lead to a more subangular to subrounded shape of the clasts (Benn & Evans 2010). This description matches with the results from the clasts in the Bee Pit (Figure 19), where they display a dominantly subangular to subrounded shape.

Regarding the maximum particle size, comparing the measured sizes of the clasts with the graph that relates distance vs. clast shape (Ashley et al. 1985), gives a notion about the proximity to the source (Figure 24). For the lower units 1 and 2, it can be pointed out that with their range of sizes they were most likely deposited in a proximal to intermediate distance, around 6 to 10 km from the source. For unit 4, there is a broader variation following the graph given the wide size range (12-60 cm). The smaller range of measurements (12-20 cm) would indicate a middle to distal distance from the source and for the middle range of sizes (20-35 cm) would be in a middle to proximal distance. The larger portion ranging from 36 to 40 cm, with a 60 cm boulder, would indicate the most proximal distance. Finally, the upper section units' measurements imply a deposition with a middle distance. Therefore, the source of the sediments from the Bee Pit is possibly in a middle to proximal distance. This is viable having the High Tatras with approximately 7-9 km distance from the study area and assuming this as the source. This assumption is supported by the geomorphological evidence that has been drawn in the literature (Figure 25) (e.g. Lindner et al. 2003; Zasadni et al. 2020).

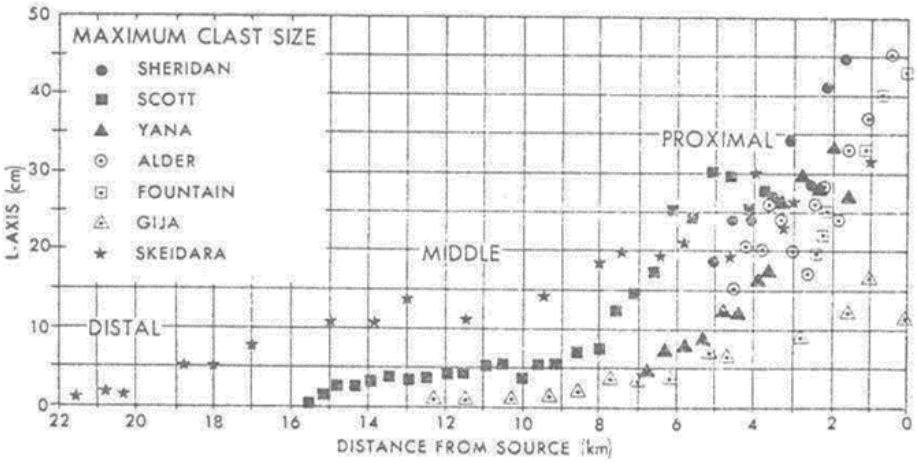

Figure 24. Diagram depicting the changes in maximum clast size (y-axis) with downstream distance from the source (x-axis), taken from Ashley et al. (1985).

Fig. 1. Limits of glaciers and glaciofluvial levels in the Tatra Mts., after Nemčok (1993*b*), simplified with later supplements

Biber Glaciation: 1 — glaciofluvial level; Donau Glaciation: 2 — glaciofluvial level; Günz Glaciation: 3 — glaciofluvial level; Mindel Glaciation: 4 — glacier limit, 5 — glaciofluvial level; pre-Riss Glaciation: 6 — glaciofluvial level; Riss I Glaciation: 7 — glacier limit, 8 — glaciofluvial level; Riss II Glaciation: 9 — glacier limit, 10 — glaciofluvial level; Würm Glaciation: 11 — glacier limit (solid line) and firn fields limit (dashed line); 12 — glaciofluvial level; Late Glacial and Early Holocene: 13 — extent of glaciers, dead ice and rock glaciers; 14 — main mountain ridges; 15 — main peaks; 16 — river valleys

Figure 25. Map of the Tatra Mountains depicting the ice extent for glaciations that took place along with their deposits, taken from Lindner et al. (2003).

Considering the previous clast shape analysis and the studies made on the evolution of the clast-roundness concerning their distance to the source, they showed that with the active transport the distance does not need to be long for significant edge-rounding to occur (Benn & Evans 2010). An explanation for the presence of these local and very large boulders could be, according to Williams (1983), the presence of high local relief, which could enhance the chances of mudflows or debris flows. Additionally, it could also be river-ice -rafted boulders, which are apt to occur on single boulders rather than in large numbers (Williams 1983). This seems to apply to the ones found in unit 4, since it was only these two, in the whole Bee Pit, to have a size bigger than 1.5 m.

Another type of deposits that seems to fit with the characteristics of the Bee Pit units would be hyperconcentrated flow deposits. This type of deposits is found in the middle between stream flow and debris flow (Mulder & Alexander 2001; Benvenuti & Martini 2002). First of all, this process forms layers that are generally matrix supported gravels, which reflect a mass transport of material and a rapid deposition. Secondly, the units from hyperconcentrated flows can be massive or display some internal structures like crude stratification, this stratification could record pulsed deposition from the surges in the flow. Similarly, the granulometry, the active transport process can produce a sediment distribution ranging from clay to pebbles, or larger, and is typically bimodal (Benn & Evans 2010), as it was noted on the coarser units of the Bee Pit. This type of distribution shows the evidence of progressive particle size reduction as the stress during shear causes the particles to fracture. The bimodal nature of the layers is caused by the effect of crushing and abrasion (Boulton 1978; Haldorsen 1981). Likewise, it is common for the texture and structures to increase upwards as an indication of a fluvial process, like sorting and well-developed bedding. This change is believed to be an indication of the transition from hyperconcentrated to normal flow, which can happen during falling discharges, as a result of formerly suspended sediments (Maizels 1989a; Maizels 1989b).

On the other hand, the finer units tend to be massive but there are some places in which certain structures were found, like in unit 3 and unit 12. In both units located on both the upper and lower sections of the Bee Pit, there seems to be planar stratification. In the case of unit 12, there is locally an erosional boundary between the sand and the overlying gravel and cobbles layer. Also, towards the southern side of the outcrop there seem to be fine sand beds, cut by the overlying gravel bed, which could be related to a local channel formation. These features are an indication of transport with a lower level of energy as compared to the coarser units. Likewise, the crossbedding and the erosion caused by the overlying layer implies a fluvial compo-

nent in the deposition. The combination of these different energy levels, producing the intercalation of fine and coarse sediments, could be related to the high-level flows previously mentioned. As mentioned in (Ashley et al. 1985), during the high flow the finer components of the sediments are in suspension and then in the following low flow after the coarse fraction has been deposited, the fines do as well. Another possible explanation for the presence of fine sediments in a high-level way of transportation, in Benn & Evans (2004) is that they could have possibly originated at the glacier bed or from pre-existing sediments in which the fine fraction could have been present. Furthermore, the sediments in suspension are also a characteristic of turbulent flows, for this to occur the flow must be directed upwards. Also, the flows could either be homogenous or have two layers where the upper one contains fine grains that have a low-concentration component and a lower one with coarse grained high concentration. The deposition is correspondingly a result of the falling shear stress and flow velocities which are associated with the reduction of stream gradient and the depth of the flow.

6.2 Luminescence dating with OSL and IRSL

6.2.1 OSL dating issues

To properly estimate the age for the samples, it was necessary to change the analysed mineral from quartz to feldspar. As shown in the previous chapter, the results for the IR/B tests from the quartz grains showed they were highly contaminated with feldspar. Even though several variations of dose estimate measurements were done on quartz, like pulsed OSL and differential OSL, none of them improved the results. This issue is related to the instability of the quartz signal components, resulting in poor quartz which is also dim. Problematic quartz leads to a high percentage of rejected aliquots and therefore reduction in the quantity of D_e values (Table 5) (Trauerstein et al. 2017). The weak fast component that the quartz samples showed is clearly related to the problem of true depositional age estimation, and also with the thermally unstable OSL signal components (Steffen et al. 2009). Therefore, when the first measurements done with feldspar showed better results, it was clear it was the correct path to take. For example, the dose recovery measurements showed an upgrade in the quality of the feldspar grains, with having ratios closer to one and smaller variations between them.

Sediment Bleaching

The problem with choosing between quartz and feldspar for luminescence dating is a quite common one. In the literature, there are many papers where scientists try to find a solution and methods with which to improve the luminescence measurements on quartz and feldspar (e.g. Ankjærgaard et al. 2010; Alexanderson & Murray 2012; Colarossi et al. 2015; Gliganic et al. 2017). In the studies where they used feldspar, as it is Colarossi et al. (2015), the post-IR IRSL signal is used to help with the issue of incomplete bleaching that sediments can present. From the comparison made of the rate to which the $pIRIR_{225}$ and $pIRIR_{290}$ signals bleach, it was concluded that for the poorly bleached fluvial sediments the $pIRIR_{225}$ signal was the most appropriate for dating. The $pIRIR_{290}$ signal takes a longer time to be bleached and considering a fluvial depositional context, it was not used. This comparison also included quartz OSL, which has a faster bleaching rate than any of the feldspar signals (Colarossi et al. 2015). It was also noted that the values of the equivalent doses were consistently larger in feldspar than in quartz, given the difference in bleaching of the two signals. This difference in the bleaching rate was also observed in the Bee Pit samples so the $pIRIR_{225}$ was preferred for dating with the feldspar grains.

It has been shown in previous studies of luminescence signals from modern sediments (Alexanderson & Murray 2012) that the nature of the depositional environment can influence the grains to be incompletely zeroed, like short transport distance and turbid water (Gliganic et al. 2017). This could lead to the sediments to be incompletely zeroed at the time of deposition. Also, proximity to the source could be a cause for obtaining higher doses than in sediments that have had longer transport and are deposited further away (King et al. 2014). In relation to the samples from the Bee Pit and the way of transport, it could be an indication for the susceptibility of the samples to present bleaching issues as well. The issue with incompletely bleached grains and the proper identification of these samples is a relevant one when dating with luminescence because the samples that have been properly bleached will give the most accurate ages (Murray et al. 2012).

6.2.2 Water content

The water content or soil moisture is related to the determination of dose rate and subsequent age estimation in luminescence dating. Given that the water within the pores of the sediment impact the density it can also alter or dilute the exposure to radiation from the surrounding sediments and cosmic rays (Banerjee et al. 2001). This occurs because the water can absorb more radiation per unit of mass than sediment with air-filling pore spaces (Nelson & Rittenour 2015). Therefore, the uncertainty that the attenuation can cause in water content could eventually introduce large errors into the OSL dating calculations (Rosenzweig & Porat 2015).

This is the reason why the water content was analysed with detail for the samples collected in the Bee Pit.

According to the suggested process of calculation for the water content in Nelson & Rittenour (2015), all the precautions were followed to estimate the values of field water content and saturated water content. These are important values since they contain data from the specific climatic conditions from the study area and they account for the variations of water content with soil depth (Rosenzweig & Porat 2015). The fact that the Bee Pit samples had different values in depth, the determination of the most likely water content for the samples was done by taking this into account. The obtained ages, calculated with these chosen values of water content, were plotted against the depth of the samples to show the variation of the ages with the position of the samples (Figure 26).

6.2.3 Anomalous fading

It is understood that even though feldspar is more favourable to be used for luminescence dating in certain situations, like the Bee Pit, there should always be caution with the anomalous fading. As it has been aforementioned and explained, it could be responsible for underestimating the doses and making the ages seem younger than they truly are, hampering their accuracy (Banerjee et al. 2001; Thiel et al. 2011a). Also, the proposed solution for avoiding the signal stability issue or fading, and the one applied in this study was to use the $pIRIR_{225}$ (Buylaert et al. 2012). This was the chosen temperature for this study, instead of other pIRIR signals like 290°C because, with higher temperature pIRIR signals, they become harder to bleach. Furthermore, in depositional environments with incomplete bleaching, it is recommended to use higher signals than IR_{50} (Colarossi et al. 2015). Also, $pIRIR_{225}$ has been proven to show much more stable signals and has been used successfully in other studies (Thiel et al. 2011b; Roberts et al. 2018).

From the results chapter, when comparing the calculated D_e values from IR_{50} and $pIRIR_{225}$ signals in Table 8A, there is a clear offset of about double in the latter. According to the literature, this is anticipated due to the differences in the stability of the signals. Consequently, the measurement of anomalous fading should be done for both signals. Nevertheless, it is taken into account that these rates are difficult to assess (Roberts et al. 2018). The judgement of the obtained g-values for both signals needs to be done carefully since it is one of the defining components to attain the correct age in the end and therefore a lot of considerations must be given. The $pIRIR_{225}$ signal has a lower fading rate and could be comparable to the fast-component dominated quartz, which as it has been mentioned before is widely used since it is believed not to fade. Furthermore, when the g-values are < 1-1.5% they are quite hard to assess (Roberts 2012). Therefore, many authors conclude that the uncorrected ages of $pIRIR_{225}$ would be more advisable to use (Buylaert et al. 2012; Roberts 2012; Buylaert et al. 2013). The high g-values of the IR_{50} signal, obtained from the Bee Pit samples, could also lead to uncertain ages. Therefore, if the corrected for fading ages were used to determine the ages, they would most likely be younger. Taking all these features into consideration the four calculated ages for the two IRSL signals, uncorrected and corrected for fading, were analysed and compared. The conclusions of this is described in detail in the next section.

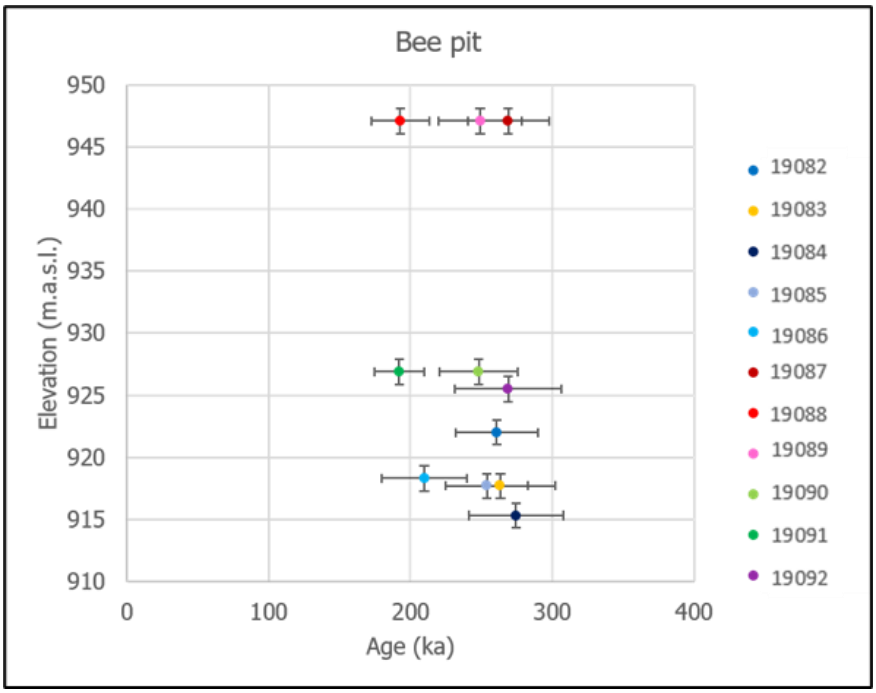

Figure 26. Graph depicting the relation of age (ka) in the x-axis vs. elevation of the sample in the outcrop in the y-axis

6.2.4 Determination of the ages

The process of estimating ages needs to take into account all the features that have been mentioned before, which have a clear impact on the final result, such as insufficient bleaching and variable dose rates during the history of the sediment due to changing water content or nuclide leaching. In this case, the dose rate is assumed to remain constant over time. As described in the literature, the uncertainty in the ages can also be influenced by random errors in the D_e values which makes the determinations difficult. (Fuchs & Owen 2008).

With the particular case of the Bee Pit samples, one way of helping in the determination was the comparison to the modern analogues analysed by van Wees (2020). This is due to the fact that a comprehensive modern analogue investigation is commonly used to confirm that the OSL signal, in modern glacial and fluvial sediments, is well bleached (King et al. 2014). Likewise, the proximity of these samples serves as a reliable confirmation for the age analysis of the study area (Table 9A). The results obtained from the analysis are depicted in Table 9B and they clearly show significant doses, although the expected value would be 0 Gy, that is not the case for these samples. Therefore, it is clear that the modern day Velická river's sediments have not been fully bleached and hence confirms a bleaching issue. The modern analogue can be considered as representative of the samples collected from the Bee Pit, with the assumption that the source of the material is similar. Moreover, the comparison of the depositional environment from the modern analogue and one of the Bee Pit would display differences such as the lack of glaciers in today's Tatra Mountains. The fact that the transport of the modern analogue would depend mostly on the river, without a glacier ice component, could be presumed as better conditions for bleaching than in the past. Consequently, it could be said that the conditions in the past probably had inferior bleaching opportunities than now.

The residual dose values determined for the Bee Pit samples were around 15 Gy in the case of pIRIR225°C (Table 6), which is lower than the doses from modern analogues and thus seems to confirm of the bleaching problem for the modern deposits. The unbleachable residual dose is, however, considered rather small and they were quite similar to each of the other samples. When the D_e value was chosen for the age calculation, the mean of the doses was therefore used without subtracting the residual dose. In several studies, it is found that the residual luminescence signals may be reduced with increasing transport distance and therefore improve the bleaching opportunities (King et al. 2014). Likewise, in the case of glacifluvial sediments, the exposure to daylight is not fully reached due to the nature of glacial waters in which the sediments are transported, characterised for being turbid. Consequently, the intensity of daylight is reduced rapidly producing ineffective bleaching in the sediments (Berger 1990). This has been proven with other modern analogues studies where the residual signal would result in age overestimations in the geological record (Fuchs & Owen 2008).

Considering the results obtained from the equivalent doses for feldspar in both the Bee Pit and the modern analogue samples, it is clear that there is a bleaching problem with the samples and they do have a residual dose probably since the time of deposition. Nevertheless, according to the referenced literature, the best option is to select the ages calculated based on the $pIRIR_{225}$. In addition to this, the majority of the samples showed saturation for 225°C, which has been stated as a suggestion for the samples to not have a significant fading (Thiel et al. 2011b). This also gives more support for the uncorrected for fading ages of $pIRIR_{225}$ as a more reliable choice.

6.3 Depositional History

The described characteristics of the deposited sediments in the Bee Pit show a clear indication of a deposition made by a high flow way of transport, which has been suggested as a possible debris flow before. However, the characteristics of the sediments also fit with the hyperconcentrated flows. Both debris flows and

Table 9. A) Data from the location of the two simples analysed for modern analogues. B) D_e values obtained from the samples, measured for both IRSL 50°C and PIRIR 225°C, modified from van Wees (2020)

A)

Sample No.	Location	Coordinates		
105	Surface	N49° 07320	E20° 10473	1043
106	Riverbed	N49° 07320	E20° 10474	1043

B)

Sample No.	IRSL 50°C		Post-IR IRSL 225°C	
	Mean De (Gy)	Error	Mean De (Gy)	Error
105	31	1.46	109	7.04
106	56	1.85	183	5.83

hyperconcentrated water flows are classified, among others, as subaerial flows (Germain & Ouellet 2013). Additionally, it is stated that the flow processes are considered as a continuum of flow conditions and sediment concentrations, which complicates the classification of the processes in only one clear way (Batalla et al. 1999). Both can occur within one single drainage channel or single flow event (Germain & Ouellet 2013). Nevertheless, an attempt to classifying them was made by comparing the studied sediments to the established sedimentological features of these deposits in the literature (e.g. Mulder & Alexander 2001; Benvenuti & Martini 2002; Benn & Evans 2010; Germain & Ouellet 2013).

Furthermore, the occurrence of hyperconcentrated flows in glacifluvial environments is quite high given that they can transport significant volumes of sediment. The capacity of flushing suspended sediment could also be recognized in seasonal variations (Swift et al. 2002). Likewise, high discharges are often associated with glacial melt streams which therefore could lead to a huge capacity to transport sediment. The discharges can also lead to channelized drainage systems, which are also characterized by high flow velocities, and can rapidly strip subglacial sediment from the flow paths. For the hyperconcentrated flows to form the rates of meltwater production need to be high so that the sediment can be evacuated quickly from beneath the glaciers and transported beyond the glacier margin (Saunderson 1977; Benn & Evans 2010). Additionally, the development of this occurs easily during the melt season (Swift 2006). Further evidence is given with the sedimentary structures found in the sand composed units because the stratification and grading are usually found in water transported deposits. Even though there was no imbrication of the clasts found, the other sedimentary structures are appointed to the transition from a hyperconcentrated to normal flow (Germain & Ouellet 2013).

The previous discussion of the depositional process indicates the context of a glacifluvial environment, which is evidenced primarily by the large amount of water and sediments deposited. Secondly, glaciers have the capacity of doing so through high flow velocities and high rates of meltwater production (Benn & Evans 2010). Therefore, the next step should be to identify in what glaciation and period the sediments from the Bee Pit were deposited. This was done by joining the sedimentology with the luminescence dating, along with the thorough process of selection for the ages of the samples. First of all, in accordance with the determination of glacifluvial deposits comes the found evidence of a glacier being present in the area. In many papers, it has been stated that in the Tatra Mountains, for both the Slovakian and Polish sides, there have been glacifluvial deposits found in different altitudes. In some cases, there were even terminal and lateral moraines, for the Mindel, Riss and Würm glaciations (e.g. Lindner et al. 2003; Makos 2015; Kłapyta et al. 2016; Zasadni et al. 2020). The composition of these moraines has been described to include strongly weathered and disintegrated granite boulders (Lindner et al. 2003), where the advanced weathering of the boulders is assumed to have occurred *in situ*. Consequently, it is appointed that these features match well with the description of the coarse units since granite is the only lithology of the cobbles and boulders fractions.

Moreover, as mentioned before, there is evidence of around eight different glaciation periods in the Tatra Mountains where the glacier ice reached different extents varying between glaciations (Figure 26). The glaciations where the ice reached greater extents were the Mindel (Sanian), Riss I (Odranian), and the Würm (Vistulian) glaciations, the latter being surprisingly large (Lindner et al. 2003). The ages from the Bee Pit, for which the bleaching issue was considered minor given the small residual dose for the $pIRIR_{225}$, were compared with the established glaciations. They coincide primarily with the Riss glaciation, which has been given ages between 228 ± 44 ka and 263 ± 36 ka in a study done on the Polish side of the Tatras (Lindner et al. 1993). Also, another argument that gives more weight to the Riss instead of the Mindel glaciation is the fact that the Mindel has been reported as being limited in the High Tatras region and mostly developed in the western Tatras. The areas with Mindel glaciation evidence are further to the eastern side of the Tatras in comparison to the Biely Váh river valley. Moreover, the presence of the glacier ice and its corresponding glacifluvial deposits during the Riss glaciation have been identified in the southern foreland of the Tatra Mountains, in the vicinity of Štrbské Pleso (Figure 26), where the moraines are found in contact with glacifluvial deposits (Lindner et al. 2003). This locates the glacier extent quite close to the study area in comparison to the Riss II glaciation. As a final point, it is also worth mentioning that the high level of weathering of the granite clasts, is in accordance with the samples being this old, and not being deposited in a younger period such as the Würm glaciation.

7 Conclusions

An abandoned gravel pit in the Biely Váh valley in the southern foothills of the High Tatra Mountains was investigated by sedimentological analyses and luminescence dating. The interpretations and discussion of the data allowed to draw the following conclusions.

- The sedimentological characteristics of the units, together with the results of clast shape and maximum particle size analysis, indicate that the deposits have been subject to high energy transport. This was assigned to subaerial flows, which includes both debris flows and hyperconcentrated flows. After analysing the main features of the sediments from the Bee Pit,

it was concluded that the glacifluvial sediments were deposited by hyperconcentrated flows.

- The luminescence dating analysis for the eleven collected samples of the study area turned out to present certain challenges. First of all, the OSL quartz analysis did not yield good results, even though several options were tried, besides the standard SAR protocol tests, like pulsed stimulation and differential OSL. The conclusion was that the quartz was highly contaminated with feldspar and suffered from signal instability and dimness, which led to the use of IRSL dating of feldspar instead.

- The age calculation with feldspar presented a better option to determine the ages for the Bee Pit samples, which was confirmed after obtaining good results from the standard quality tests. Nevertheless, the use of feldspar has certain risks such as incomplete bleaching of the grains and fading. These risks were managed by determining the g-value and the level of residual dose in the grains. Including the use of IRSL 50°C and post-IR IRSL 225°C signals, where the latter have been proven to be better for samples with a complex way of transport, leading to incomplete bleaching. Furthermore, when comparing the data from the modern analogues with the obtained results it was assumed that, even though there is a bleaching issue in the modern sediments, the residual dose from the samples was rather small and not considered risky for the dating.

- Regarding the fading, the determined g-values for the post-IR IRSL 225°C were considered acceptable, having values <1-1.5 %/decade. Similarly, after the water content was determined for the samples, four ages were calculated for each sample. Therefore, each sample had an age for both IRSL 50°C and post -IR IRSL 225°C signals, with and without correction for fading. The ages uncorrected for fading from the post-IR IRSL 225°C were selected as the most reliable ages for the Bee Pit samples, given that it is the ones that best fit the characteristics of proper age determination.

- It is known that eight glaciations have taken place in the Tatra Mountains with the geomorphological evidence being the presence of glacifluvial deposits and moraines. Therefore, a correlation was made between the obtained ages from the Bee Pit and the proposed ages of these glaciations. Considering the granite lithology of the clasts, their high degree of weathering, characteristics of the sediments and that the ages of the samples ranging between 200 and 260 ka, they were placed within the Riss glaciation. These ages agree well with thermoluminescence ages between 228 ± 44 ka and 287 ± 43 ka from glacifluvial deposits, also correlated to the Riss glaciation, on the northern side of the Tatra mountains (Lindner et al. 2003). Besides, the sediments at the Bee Pit share characteristics, such as weathered granite boulders with sand and gravel material, with glacifluvial sediments in the vicinity of Štrbské Pleso and that have been correlated to the Riss glaciation (Lindner et al. 2003). In conclusion, the results indicate that the glacifluvial sediments, deposited in the Biely Váh river valley, were formed during the Riss glaciation by means of hyperconcentrated flows.

8 Acknowledgments

I want to thank the Geology department for the support given during my thesis and for funding the amazing experience of working in the Tatra Mountains. Also, to express my gratitude to my supervisor Helena Alexanderson who always helped me with every step of the process. As well as to my co-supervisors Isa Doverbratt and Juraj Janocko for their special assistance in the laboratory and fieldwork.
I want to acknowledge the Nordic laboratory for Luminescence Dating Risö, in Denmark for providing the facilities and support with the dose rate estimation.
The completion of this Master was the result of the endless encouragement from my family and friends, who regardless of the distance were always close. Especially from my parents who have constantly encouraged me to accomplish my goals.
I want to express my gratitude to my classmates who became very good friends almost from the beginning of our studies and were a very important part of my great experience in Sweden. Expressly to Roos van Wess who worked on a parallel project to mine and was a great support throughout the whole process.

References

Aitken, M. J., 1998: *Introduction to optical dating: the dating of Quaternary sediments by the use of photon-stimulated luminescence*. Clarendon Press.

Alexanderson, H. & Murray, A. S., 2012: Luminescence signals from modern sediments in a glaciated bay, NW Svalbard: *Quaternary Geochronology 10*, 250-256.

Ankjærgaard, C., Jain, M., Thomsen, K. J. & Murray, A., 2010: Optimising the separation of quartz and feldspar optically stimulated luminescence using pulsed excitation: *Radiation measurements 45*, 778-785.

Ashley, G. M., Shaw, J. & Smith, N. D., 1985: *Glacial sedimentary environments*. Sepm Society for Sedimentary Formations. 85-133 sid.

Ballantyne, C. K., 1982: Aggregate clast form characteristics of deposits near the margins of four glaciers in the Jotunheimen Massif, Norway: *Norwegian Journal of Geography,* 36 Issue 2, 103-110.

Banerjee, D., Murray, A. S., Bøtter-Jensen, L. & Lang, A., 2001: Equivalent dose estimation using a single aliquot of polymineral fine grains: *Radiation measurements 33*, 73-94.

Batalla, R., De Jong, C., Ergenzinger, P. & Sala, M., 1999: Field observations on hyperconcentrated flows in mountain torrents: *Earth Surface Processes and Landforms: The Journal of the British Geomorphological Research Group 24*, 247-253.

Bateman, M., 2019: Handbook of luminescence dating. Caithness: Whittles.

Benn, D. I. & Evans, D. J. A. 2010: Glaciers and Glaciation. 802 pp. Arnold, London.

Benn, D. I. & Ballantyne, C. K., 1993: The description and representation of particle shape: *Earth Surface Processes and Landforms 18*, 665-672.

Benn, D. I. & Ballantyne, C. K., 1994: Reconstructing the transport history of glacigenic sediments: a new approach based on the co-variance of clast form indices: *Sedimentary Geology 91*, 215-227.

Benvenuti, M. & Martini, I., 2002: Analysis of terrestrial hyperconcentrated flows and their deposit: *Flood and megaflood processes and deposits: recent and ancient examples*, 167-193.

Berger, G. W., 1990: Effectiveness of natural zeroing of the thermoluminescence in sediments: *Journal of Geophysical Research: Solid Earth 95*, 12375-12397.

Bøtter-Jensen, L., Andersen, C., Duller, G. A. & Murray, A. S., 2003: Developments in radiation, stimulation and observation facilities in luminescence measurements: *Radiation measurements 37*, 535-541.

Bøtter-Jensen, L., Bulur, E., Duller, G. & Murray, A., 2000: Advances in luminescence instrument systems: *Radiation measurements 32*, 523-528.

Boulton, G., 1978: Boulder shapes and grain-size distributions of debris as indicators of transport paths through a glacier and till genesis: *Sedimentology 25*, 773-799.

Brook, M. & Lukas, S., 2012: Lithological and fluvial influences on clast shape measurements in a temperate alpine environment: a case study from Fox Glacier, New Zealand. *EGU General Assembly Conference Abstracts.* 1539 s.

Buylaert, J.-P., Murray, A., Gebhardt, A., Sohbati, R., Ohlendorf, C., Thiel, C., Wastegård, S., Zolitschka, B. & Team, T. P. S., 2013: Luminescence dating of the PASADO core 5022-1D from Laguna Potrok Aike (Argentina) using IRSL signals from feldspar: *Quaternary Science Reviews 71*, 70-80.

Buylaert, J.-P., Murray, A. S., Thomsen, K. J. & Jain, M., 2009: Testing the potential of an elevated temperature IRSL signal from K -feldspar: *Radiation measurements 44*, 560-565.

Buylaert, J. P., Jain, M., Murray, A. S., Thomsen, K. J., Thiel, C. & Sohbati, R., 2012: A robust feldspar luminescence dating method for Middle and Late P leistocene sediments: *Boreas 41*, 435-451.

Colarossi, D., Duller, G., Roberts, H., Tooth, S. & Lyons, R., 2015: Comparison of paired quartz OSL and feldspar post-IR IRSL dose distributions in poorly bleached fluvial sediments from South Africa: *Quaternary Geochronology 30*, 233-238.

Duller, G., 2003: Distinguishing quartz and feldspar in single grain luminescence measurements: *Radiation measurements 37*, 161-165.

Duller, G., 2018: Enhancing Analyst by integrating the R package'Luminescence': *Ancient TL 36*, 1-6.

Duller, G. A., 2008: Luminescence Dating: guidelines on using luminescence dating in archaeology: *English Heritage,* 47 pp.

Durcan, J. A., King, G. E. & Duller, G. A., 2015: DRAC: Dose Rate and Age Calculator for trapped charge dating: *Quaternary Geochronology 28*, 54-61.

Evans, D. J. & Benn, D. I., 2014: *A practical guide to the study of glacial sediments*. Routledge.

Eyles, N., Eyles, C. H. & Miall, A. D., 1983: Lithofacies types and vertical profile models; an alternative approach to the description and environmental interpretation of glacial diamict and diamictite sequences: *Sedimentology 30*, 393-410.

Fuchs, M. & Owen, L. A., 2008: Luminescence dating of glacial and associated sediments: review, recommendations and future directions: *Boreas 37*, 636-659.

Germain, D. & Ouellet, M.-A., 2013: Subaerial sediment-water flows on hillslopes: Essential research questions and classification challenges: *Progress in Physical Geography 37*, 813-833.

Gliganic, L. A., Cohen, T. J., Meyer, M. & Molenaar, A., 2017: Variations in luminescence properties of quartz and feldspar from modern fluvial sediments in three rivers: *Quaternary Geochronology 41*, 70 -82.

Graham, D. J. & Midgley, N. G., 2000: Graphical representation of particle shape using triangular diagrams: an Excel spreadsheet method: *Earth Surface Processes and Landforms 25*, 1473-1477.

Haldorsen, S., 1981: Grain-size distribution of subglacial till and its realtion to glacial scrushing and abrasion: *Boreas 10*, 91-105.

Hanzel, V., Gazda, S. & Vałkovskð, I., 1984: Hydrogeológia jušnej časti Vysokðch Tatier a ich predpolia.[Hydrogeology of the southern part of High Tatra Mts. and its foreland]: *Záp. Karpaty, Sér. Hydrogeol. a Inš. Geol 5*.

Huntley, D., 2001: Some notes on language: *Ancient TL 19*, 27-28.

Huntley, D. J. & Lamothe, M., 2001: Ubiquity of anomalous fading in K-feldspars and the measurement and correction for it in optical dating: *Canadian Journal of Earth Sciences 38*, 1093-1106.

Jain, M., Murray, A., Bøtter-Jensen, L. & Wintle, A., 2005: A single-aliquot regenerative-dose method based on IR (1.49 eV) bleaching of the fast OSL component in quartz: *Radiation measurements 39*, 309-318.

King, G. E., Sanderson, D. C., Robinson, R. A. & Finch, A. A., 2014: Understanding processes of sediment bleaching in glacial settings using a portable OSL reader: *Boreas 43*, 955-972.

Kłapyta, P., Zasadni, J., Pociask-Karteczka, J., Gajda, A. & Franczak, P., 2016: Late Glacial and Holocene paleoenvironmental records in the Tatra Mountains, East-Central Europe, based on lake, peat bog and colluvial sedimentary data: A summary review: *Quaternary International 415*, 126-144.

Knoll, G. F., 1979: Radiation detection and measurement(Book): *New York, John Wiley and Sons, Inc., 1979. 831 p*.

Kotarba, A., 2007: Geomorphic activity of debris flows in the Tatra Mts. and in other European mountains: *Geographia Polonica 80*, 137-150.

Králiková, S., Vojtko, R., Sliva, U., Minár, J., Fügenschuh, B., Kováč, M. & Hók, J., 2014: Cretaceous—Quaternary tectonic evolution of the Tatra Mts (Western Carpathians): constraints from structural, sedimentary, geomorphological, and fission track data: *Geologica Carpathica 65*, 307-326.

Krüger, J. & Kjær, K. H., 1999: A data chart for field description and genetic interpretation of glacial diamicts and associated sediments… with examples from Greenland, Iceland, and Denmark: *Boreas 28*, 386-402.

Lawson, M. J., Roder, B. J., Stang, D. M. & Rhodes, E. J., 2012: OSL and IRSL characteristics of quartz and feldspar from southern California, USA: *Radiation measurements 47*, 830-836.

Lian, O. B., 2007: *Optically-Stimulated Luminescence*. Elsevier, Inc. 1491 sid.

Lindner, L., Dzierżek, J., Marciniak, B. & Nitychoruk, J., 2003: Outline of Quaternary glaciations in the Tatra Mts.: their development, age and limits: *Geological Quarterly 47*, 269-280.

Lindner, L., Nitychoruk, J. & Butrym, J., 1993: The problem of number and age of glaciations in the Tatra Mts. against thermoluminescence dating of glaciofluvial sediments of the Biały Dunajec drainage basin: *Przegl. Geol 41*, 10-21.

Lukas, S., Benn, D. I., Boston, C. M., Brook, M., Coray, S., Evans, D. J., Graf, A., Kellerer-Pirklbauer, A., Kirkbride, M. P. & Krabbendam, M., 2013: Clast shape analysis and clast transport paths in glacial environments: A critical review of methods and the role of lithology: *Earth-Science Reviews 121*, 96-116.

Maizels, J., 1989a: Sedimentology and palaeohydrology of Holocene flood deposits in front of a jökulhlaup glacier, South Iceland. *Floods, hydrological, sedimentological and geomorphological implications. Workshop, joint meeting of the BGRG*

and the British Hydrological Society. 239 -251 s.

Maizels, J., 1989b: Sedimentology, paleoflow dynamics and flood history of jokulhlaup deposits; paleohydrology of Holocene sediment sequences in southern Iceland sandur deposits: *Journal of sedimentary research 59*, 204-223.

Makos, M., 2015: Deglaciation of the high Tatra mountains: *Cuadernos de Investigación Geográfica 41*, 317-335.

Makos, M., Dzierżek, J., Nitychoruk, J. & Zreda, M., 2014: Timing of glacier advances and climate in the High Tatra Mountains (Western Carpathians) during the Last Glacial Maximum: *Quaternary Research 82*, 1-13.

Makos, M., Nitychoruk, J. & Zreda, M., 2013: Deglaciation chronology and paleoclimate of the Pięciu Stawów Polskich/ Roztoki Valley, high Tatra Mountains, Western Carpathians, since the Last Glacial Maximum, inferred from ^{36}Cl exposure dating and glacier–climate modelling: *Quaternary International 293*, 63-78.

Mulder, T. & Alexander, J., 2001: The physical character of subaqueous sedimentary density flows and their deposits: *Sedimentology 48*, 269-299.

Murray, A., Thomsen, K. J., Masuda, N., Buylaert, J.-P. & Jain, M., 2012: Identifying well-bleached quartz using the different bleaching rates of quartz and feldspar luminescence signals: *Radiation measurements 47*, 688-695.

Murray, A. S. & Wintle, A. G., 2000: Luminescence dating of quartz using an improved single-aliquot regenerative-dose protocol: *Radiation measurements 32*, 57-73.

Murray, A. S. & Wintle, A. G., 2003: The single aliquot regenerative dose protocol: potential for improvements in reliability: *Radiation measurements 37*, 377-381.

Nelson, M. S. & Rittenour, T. M., 2015: Using grain-size characteristics to model soil water content: Application to dose-rate calculation for luminescence dating: *Radiation measurements 81*, 142-149.

Rhodes, E. J., 2011: Optically stimulated luminescence dating of sediments over the past 200,000 years: *Annual Review of Earth and Planetary Sciences 39*, 461-488.

Roberts, H. M., 2012: Testing Post-IR IRSL protocols for minimising fading in feldspars, using Alaskan loess with independent chronological control: *Radiation measurements 47*, 716-724.

Roberts, H. M., Bryant, C. L., Huws, D. G. & Lamb, H. F., 2018: Generating long chronologies for lacustrine sediments using luminescence dating: a 250,000 year record from Lake Tana, Ethiopia: *Quaternary Science Reviews 202*, 66-77.

Rosenzweig, R. & Porat, N., 2015: Evaluation of soil-moisture content for OSL dating using an infiltration model: *Ancient TL 33*, 10-14.

Saunderson, H. C., 1977: The sliding bed facies in esker sands and gravels: a criterion for full-pipe (tunnel) flow?: *Sedimentology 24*, 623-638.

Sneed, E. D. & Folk, R. L., 1958: Pebbles in the lower Colorado River, Texas a study in particle morphogenesis: *The Journal of Geology 66*, 114-150.

Steffen, D., Preusser, F. & Schlunegger, F., 2009: OSL quartz age underestimation due to unstable signal components: *Quaternary Geochronology 4*, 353-362.

Swift, D. A., 2006: Haut Glacier d'Arolla, Switzerland: Hydrological Controls on Basal Sediment Evacuation and Glacial Erosion: *Glacier Science and Environmental Change*, 23-25.

Swift, D. A., Nienow, P. W., Spedding, N. & Hoey, T. B., 2002: Geomorphic implications of subglacial drainage configuration: rates of basal sediment evacuation controlled by seasonal drainage system evolution: *Sedimentary Geology 149*, 5-19.

Thiel, C., Buylaert, J.-P., Murray, A., Terhorst, B., Hofer, I., Tsukamoto, S. & Frechen, M., 2011a: Luminescence dating of the Stratzing loess profile (Austria)–Testing the potential of an elevated temperature post-IR IRSL protocol: *Quaternary International 234*, 23-31.

Thiel, C., Buylaert, J.-P., Murray, A. S. & Tsukamoto, S., 2011b: On the applicability of post-IR IRSL dating to Japanese loess: *Geochronometria 38*, 369.

Thomsen, K. J., Murray, A. S., Jain, M. & Bøtter-Jensen, L., 2008: Laboratory fading rates of various luminescence signals from feldspar-rich sediment extracts: *Radiation measurements 43*, 1474-1486.

Trauerstein, M., Lowick, S. E., Preusser, F. & Veit, H., 2017: Testing the suitability of dim sedimentary quartz from northern Switzerland for OSL burial dose estimation: *Geochronometria 44*, 66-76.

van Wees, R. 2020. *Combining luminescence dating and sedimentary analysis to derive the landscape dynamics of the Velická Valley in the High Tatra Mountains, Slo-*

vakia. Msc thesis No. 586, Lund University.

Williams, G. P., 1983: Paleohydrological methods and some examples from Swedish fluvial environments: I cobble and boulder deposits: *Geografiska Annaler: Series A, Physical Geography 65***,** 227-243.

Wintle, A. G. & Murray, A. S., 2006: A review of quartz optically stimulated luminescence characteristics and their relevance in single-aliquot regeneration dating protocols: *Radiation measurements 41***,** 369-391.

Zasadni, J. & Kłapyta, P., 2014: The Tatra Mountains during the last glacial maximum: *Journal of Maps 10***,** 440-456.

Zasadni, J., Kłapyta, P., Broś, E., Ivy-Ochs, S., Świąder, A., Christl, M. & Balážovičová, L., 2020: Latest Pleistocene glacier advances and post-Younger Dryas rock glacier stabilization in the Mt. Kriváň group, High Tatra Mountains, Slovakia: *Geomorphology***,** 107093.

Appendixes

Appendix A. Development of the Tatra Mountains with lithostratigraphy, paleostress, where SM: sedimentary marks showing paleocurrents, TR: tectonic regime. Taken from (Králiková et al. 2014).

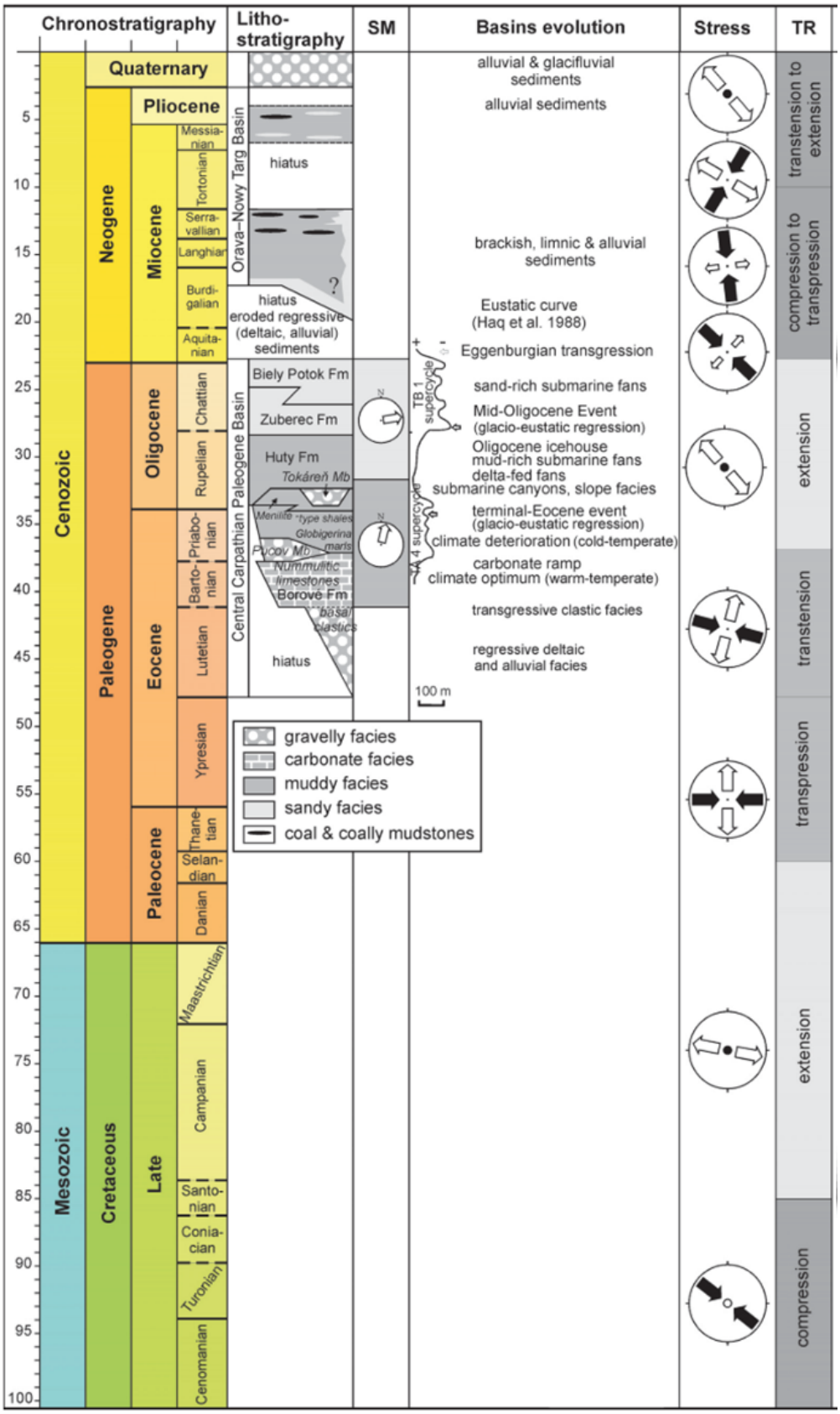

Appendix B. List of the eleven collected samples for OSL with their corresponding coordinates and units.

Sample No.	Lab No.	Latitude	Longitude	Altitude	Unit
BP-OSL-1	19082	49.09985	20.01767	922.0	Unit 3
BP-OSL-2	19083	49.09988	20.01760	917.7	Unit 1B
BP-OSL-3	19084	49.09980	20.01764	915.3	Unit 3
BP-OSL-4	19085	49.09988	20.01760	917.7	Unit 3
BP-OSL-5	19086	49.10009	20.01751	918.3	Unit 3
BP-OSL-6	19087	49.09940	20.01677	947.1	Unit 12
BP-OSL-7	19088	49.09940	20.01677	947.1	Unit 12
BP-OSL-8	19089	49.09940	20.01677	947.1	Unit 12
BP-OSL-9	19090	49.09981	20.01751	926.9	Unit 9
BP-OSL-10	19091	49.09981	20.01751	926.9	Unit 9
BP-OSL-11	19092	49.09983	20.01756	925.5	Unit 5

Tidigare skrifter i serien ”Examensarbeten i Geologi vid Lunds universitet”:

535. Zachén, Gabriel, 2018: Mesosideriter – redogörelse av bildningsprocesser samt SEM-analys av Vaca Muertameteoriten. (15 hp)
536. Fägersten, Andreas, 2018: Lateral variability in the quantification of calcareous nannofossils in the Upper Triassic, Austria. (15 hp)
537. Hjertman, Anna, 2018: Förutsättningar för djupinfiltration av ytvatten från Ivösjön till Kristianstadbassängen. (15 hp)
538. Lagerstam, Clarence, 2018: Varför svalde svanödlor (Reptilia, Plesiosauria) stenar? (15 hp)
539. Pilser, Hannes, 2018: Mg/Ca i bottenlevande foraminiferer, särskilt med avseende på temperaturer nära 0°C. (15 hp)
540. Christiansen, Emma, 2018: Mikroplast på och i havsbotten - Utbredningen av mikroplaster i marina bottensediment och dess påverkan på marina miljöer. (15 hp)
541. Staahlnacke, Simon, 2018: En sammanställning av norra Skånes prekambriska berggrund. (15 hp)
542. Martell, Josefin, 2018: Shock metamorphic features in zircon grains from the Mien impact structure - clues to conditions during impact. (45 hp)
543. Chitindingu, Tawonga, 2018: Petrological characterization of the Cambrian sandstone reservoirs in the Baltic Basin, Sweden. (45 hp)
544. Chonewicz, Julia, 2018: Dimensionerande vattenförbrukning och alternativa vattenkvaliteter. (15 hp)
545. Adeen, Lina, 2018: Hur lämpliga är de geofysiska metoderna resistivitet och IP för kartläggning av PFOS? (15 hp)
546. Nilsson Brunlid, Anette, 2018: Impact of southern Baltic sea-level changes on landscape development in the Verkeån River valley at Haväng, southern Sweden, during the early and mid Holocene. (45 hp)
547. Perälä, Jesper, 2018: Dynamic Recrystallization in the Sveconorwegian Frontal Wedge, Småland, southern Sweden. (45 hp)
548. Artursson, Christopher, 2018: Stratigraphy, sedimentology and geophysical assessment of the early Silurian Halla and Klinteberg formations, Altajme core, Gotland, Sweden. (45 hp)
549. Kempengren, Henrik, 2018: Att välja den mest hållbara efterbehandlingsmetoden vid sanering: Applicering av beslutsstödsverktyget SAMLA. (45 hp)
550. Andreasson, Dagnija, 2018: Assessment of using liquidity index for the approximation of undrained shear strength of clay tills in Scania. (45 hp)
551. Ahrenstedt, Viktor, 2018: The Neoproterozoic Visingsö Group of southern Sweden: Lithology, sequence stratigraphy and provenance of the Middle Formation. (45 hp)
552. Berglund, Marie, 2018: Basaltkuppen - ett spel om mineralogi och petrologi. (15 hp)
553. Hernnäs, Tove, 2018: Garnet amphibolite in the internal Eastern Segment, Sveconorwegian Province: monitors of metamorphic recrystallization at high temperature and pressure during Sveconorwegian orogeny. (45 hp)
554. Halling, Jenny, 2019: Characterization of black rust in reinforced concrete structures: analyses of field samples from southern Sweden. (45 hp)
555. Stevic, Marijana, 2019: Stratigraphy and dating of a lake sediment record from Lyngsjön, eastern Scania - human impact and aeolian sand deposition during the last millennium. (45 hp)
556. Rabanser, Monika, 2019: Processes of Lateral Moraine Formation at a Debris-covered Glacier, Suldenferner (Vedretta di Solda), Italy. (45 hp)
557. Nilsson, Hanna, 2019: Records of environmental change and sedimentation processes over the last century in a Baltic coastal inlet. (45 hp)
558. Ingered, Mimmi, 2019: Zircon U-Pb constraints on the timing of Sveconorwegian migmatite formation in the Western and Median Segments of the Idefjorden terrane, SW Sweden. (45 hp)
559. Hjorth, Ingeborg, 2019: Paleomagnetisk undersökning av vulkanen Rangitoto, Nya Zeeland, för att bestämma dess utbrottshistoria. (15 hp)
560. Westberg, Märta, 2019: Enigmatic wormlike fossils from the Silurian Waukesha Lagerstätte, Wisconsin, USA. (15 hp)
561. Björn, Julia, 2019: Undersökning av påverkan på hydraulisk konduktivitet i förorenat område efter in situ-saneringsförsök. (15 hp)
562. Faraj, Haider, 2019: Tolkning av georadarprofiler över grundvattenmagasinet Verveln - Gullringen i Kalmar län. (15 hp)
563. Bjermo, Tim, 2019: Eoliska avlagringar och vindriktningar under holocen i och kring Store Mosse, södra Sverige. (15 hp)
564. Langkjaer, Henrik, 2019: Analys av Östergötlands kommande grundvattenresurser ur ett klimtperspektiv - med fokus på förstärkt grundvattenbildning. (15 hp)

565. Johansson, Marcus, 2019: Hur öppet var landskapet i södra Sverige under Atlantisk tid? (15 hp)
566. Molin, Emmy, 2019: Litologi, sedimentologi och kolisotopstratigrafi över krita–paleogen-gränsintervallet i borrningen Limhamn-2018. (15 hp)
567. Schroeder, Mimmi, 2019: The history of European hemp cultivation. (15 hp)
568. Damber, Maja, 2019: Granens invandring i sydvästa Sverige, belyst genom pollenanalys från Skottenesjön. (15 hp)
569. Lundgren Sassner, Lykke, 2019: Strandmorfologi, stranderosion och stranddeposition, med en fallstudie på Tylösand sandstrand, Halland. (15 hp)
570. Greiff, Johannes, 2019: Mesozoiska konglomerat och Skånes tektoniska utveckling. (15 hp)
571. Persson, Eric, 2019: An Enigmatic Cerapodian Dentary from the Cretaceous of southern Sweden. (15 hp)
572. Aldenius, Erik, 2019: Subsurface characterization of the Lund Sandstone – 3D model of the sandstone reservoir and evaluation of the geoenergy storage potential, SW Skåne, South Sweden. (45 hp)
573. Juliusson, Oscar, 2019: Impacts of subglacial processes on underlying bedrock. (15 hp)
574. Sartell, Anna, 2019: Metamorphic paragenesis and P-T conditions in garnet amphibolite from the Median Segment of the Idefjorden Terrane, Lilla Edet. (15 hp)
575. Végvári, Fanni, 2019: Vulkanisk inverkan på klimatet och atmorsfärcirkulationen: En litterarurstudie som jämför vulkanism på låg respektive hög latitud. (15 hp)
576. Gustafsson, Jon, 2019: Petrology of platinum-group element mineralization in the Koillismaa intrusion, Finland. (45 hp)
577. Wahlquist, Per, 2019: Undersökning av mindre förkastningar för vattenuttag i sedimentärt berg kring Kingelstad och Tjutebro. (15 hp)
578. Gaitan Valencia, Camilo Esteban, 2019: Unravelling the timing and distribution of Paleoproterozoic dyke swarms in the eastern Kaapvaal Craton, South Africa. (45 hp)
579. Eggert, David, 2019: Using Very-Low-Frequency Electromagnetics (VLF-EM) for geophysical exploration at the Albertine Graben, Uganda - A new CAD approach for 3D data blending. (45 hp)
580. Plan, Anders, 2020: Resolving temporal links between the Högberget granite and the Wigström tungsten skarn deposit in Bergslagen (Sweden) using trace elements and U-Pb LA-ICPMS on complex zircons. (45 hp)
581. Pilser, Hannes, 2020: A geophysical survey in the Chocaya Basin in the central Valley of Cochabamba, Bolivia, using ERT and TEM. (45 hp)
582. Leopardi, Dino, 2020: Temporal and genetical constraints of the Cu-Co Vena-Dampetorp deposit, Bergslagen, Sweden. (45 hp)
583. Lagerstam Lorien, Clarence, 2020: Neck mobility versus mode of locomotion – in what way did neck length affect swimming performance among Mesozoic plesiosaurs (Reptilia, Sauropterygia)? (45 hp)
584. Davies, James, 2020: Geochronology of gneisses adjacent to the Mylonite Zone in southwestern Sweden: evidence of a tectonic window? (45 hp)
585. Foyn, Alex, 2020: Foreland evolution of Blåisen, Norway, over the course of an ablation season. (45 hp)
586. van Wees, Roos, 2020: Combining luminescence dating and sedimentary analysis to derive the landscape dynamics of the Velická Valley in the High Tatra Mountains, Slovakia. (45 hp)
587. Rettig, Lukas, 2020: Implications of a rapidly thinning ice-margin for annual moraine formation at Gornergletscher, Switzerland. (45 hp)
588. Bejarano Arias, Ingrid, 2020: Determination of depositional environment and luminescence dating of Pleistocene deposits in the Biely Váh valley, southern foothills of the Tatra Mountains, Slovakia. (45 hp)

LUNDS UNIVERSITET

Geologiska institutionen
Lunds universitet
Sölvegatan 12, 223 62 Lund